



**HAL**  
open science

## An Index to Distinguish Surface- and Subsurface-Intensified Vortices from Surface Observations

C. Assassi, Yves Morel, Frédéric Vandermeirsch, Alexis Chaigneau, C. Pegliasco, Rosemary Morrow, François Colas, S. Fleury, Xavier Carton, Patrice Klein, et al.

► **To cite this version:**

C. Assassi, Yves Morel, Frédéric Vandermeirsch, Alexis Chaigneau, C. Pegliasco, et al.. An Index to Distinguish Surface- and Subsurface-Intensified Vortices from Surface Observations. *Journal of Physical Oceanography*, 2016, 46 (8), pp.2529-2552. 10.1175/JPO-D-15-0122.1 . hal-02349722

**HAL Id: hal-02349722**

**<https://hal.science/hal-02349722>**

Submitted on 5 Nov 2019

**HAL** is a multi-disciplinary open access archive for the deposit and dissemination of scientific research documents, whether they are published or not. The documents may come from teaching and research institutions in France or abroad, or from public or private research centers.

L'archive ouverte pluridisciplinaire **HAL**, est destinée au dépôt et à la diffusion de documents scientifiques de niveau recherche, publiés ou non, émanant des établissements d'enseignement et de recherche français ou étrangers, des laboratoires publics ou privés.

# **An index to distinguish surface and subsurface intensified vortices from surface observations.**

**C. Assassi<sup>1,2</sup>, Y. Morel<sup>1</sup>, F. Vandermeirsch<sup>2</sup>, A. Chaigneau<sup>1</sup>, C. Pegliasco<sup>1</sup>, R. Morrow<sup>1</sup>, F. Colas<sup>4</sup>, S. Fleury<sup>1</sup>, X. Carton<sup>3</sup>, P. Klein<sup>3</sup>, R. Cambra<sup>1</sup>,**

1) LEGOS, University of Toulouse, CNES, CNRS, IRD, UPS, 14 av. Edouard Belin, 31400  
Toulouse, FRANCE

2) Ifremer, DYNECO/PHYSED, Centre de Brest, BP 70, 29280 Plouzané, France

3) LPO (CNRS/Ifremer/IRD/UBO), BP 70, 29280 Plouzané, France

4) LOCEAN (IRD/IPSL/UPMC), Paris, France.

Manuscript accepted in Journal of Physical Oceanography

DOI: 10.1175/JPO-D-15-0122.1

Corresponding author's email address: [cassassi@ifremer.fr](mailto:cassassi@ifremer.fr)

## **ABSTRACT**

In this study, we first show that it is difficult to reconstruct the vertical structure of vortices using only surface observations. In particular we show that the recent SQG and ISQG methods systematically lead to surface intensified vortices and those subsurface intensified vortices are thus not correctly modelled.

We then investigate the possibility to distinguish between surface and subsurface intensified eddies from surface data only, using the sea surface height and the sea surface temperature available from satellite observations. A simple index, based on the ratio of the sea surface temperature anomaly and the sea level anomaly, is proposed. While the index is expected to give perfect results for isolated vortices, we show that in a complex environment, errors can be expected, in particular when strong currents exist in the vicinity of the vortex. The validity of the index is then analysed using results from a realistic regional circulation model of the Peru-Chile upwelling system, where both surface and subsurface eddies coexist.

We find that errors are mostly associated with double core eddies (aligned surface and subsurface cores) and that the index can be useful to determine the nature of mesoscale eddies (surface or subsurface- intensified) from surface (satellite) observations. The errors however reach 24% and some possible improvements of the index calculations are discussed.

## 32 **Keywords**

33 Eddies, vortices, subsurface, sea surface height, sea surface density and sea surface temperature.

## 34 **1. Introduction**

35 Superimposed on the large-scale circulation, the ocean is filled with numerous  
36 coherent mesoscale eddies whose size typically corresponds to the Rossby radius of  
37 deformation between 10 and 300 km (*e.g.* Chelton *et al.*, 2007; 2011; Morrow and Le Traon,  
38 2012). Cyclonic and anticyclonic eddies can advect parcels of trapped fluid over time scales  
39 from weeks to months, and hence play an important role for the large-scale transfer and  
40 redistribution of heat, salt and momentum (*e.g.* Wunsch, 1999; Jayne and Marotzke, 2002;  
41 Morrow and Le Traon, 2012 ; Treguier *et al.*, 2012). At local scale, eddies have important  
42 implications on tracer dispersion, ocean stirring, and mixing processes (d'Ovidio *et al.*, 2004;  
43 Pasquero *et al.*, 2005; Beron-Vera *et al.*, 2008; 2010). Through horizontal and vertical  
44 motions they also affect biogeochemical properties such as nutrients and phytoplankton  
45 concentration and can thus impact biological resources and marine ecosystems (McGillicuddy  
46 and Robinson, 1997; Abraham, 1998; Martin and Richards, 2001; Lévy and Klein, 2004;  
47 Pasquero *et al.*, 2005; Bracco *et al.*, 2009). Finally, ocean eddies can also influence the lower-  
48 atmosphere winds (Chelton and Xie, 2010; Chelton, 2013), cloud cover and rainfall (Frenger  
49 *et al.*, 2013) and enhance the dissipation of energy introduced by the wind to the ocean (Munk  
50 and Wunsch, 1998; Wunsch and Ferrari, 2004).

51 Satellite-based sensing provides sea-surface parameters at increasing precision,  
52 resolution and frequencies that are crucial for studying the ocean mesoscale dynamics. Eddies  
53 are associated with thermodynamical anomalies with relatively large amplitudes and can have  
54 clear signatures on altimetry sea-level anomaly (SLA) maps and infrared sea-surface  
55 temperature (SST) images. Mesoscale vortices can be simply classified into four distinct  
56 categories depending on their rotation sense (cyclonic or anticyclonic) and the vertical  
57 position of their potential vorticity (PV) core (surface or subsurface-intensified) depending  
58 whether their core –or area where their potential vorticity reaches its maximum- is located  
59 inside the water column rather than in the surface layer. The rotation sense can be easily  
60 retrieved from SLA satellite data considering the geostrophic approximation (Pedlosky, 1987;  
61 Cushman-Roisin and Beckers, 2011). In contrast, surface satellite data do not allow, a priori,  
62 determining whether an eddy is surface or subsurface-intensified. Using in-situ hydrographic  
63 data, subsurface eddies have been observed in various sites of the World Ocean such as the

64 Mediterranean water eddies (Meddies) and Slope Water Oceanic eddies (Swoddies) in the  
65 North-East Atlantic (Pingree *et al.*, 1992a, b; Paillet *et al.*, 2002; Bashmachnikov *et al.*, 2013),  
66 the California Undercurrent eddies (Cuddies) in the North-East Pacific (Garfield *et al.*, 1999),  
67 or subsurface anticyclones in the South-East Pacific (Johnson and McTaggart, 2010;  
68 Chaigneau *et al.*, 2011; Morales *et al.*, 2012; Stramma *et al.*, 2013). Subsurface intensified  
69 eddies, that are thus ubiquitous in the ocean, are typically centred between 200 and 1000 m  
70 depth and exhibit, by nature, a completely distinct vertical structure than surface-intensified  
71 vortices (*e.g.* Chaigneau *et al.*, 2011; Colas *et al.*, 2012).

72 Different mechanism of generation can explain the formation of surface or subsurface  
73 cyclones and anticyclones. Barotropic and baroclinic instabilities of oceanic currents are  
74 known to generate anticyclone and cyclone dipoles (see, Cushman-Roisin and Beckers, 2011;  
75 Morel and McWilliams, 2001). They can also be forced by the rough floor topography  
76 (Pingree and Le Cann, 1992a; Chérubin *et al.*, 2000; Thompson, 2008). Many remote sensing  
77 observations have also revealed the formation of surface eddies in the lee of islands (Calil *et*  
78 *al.*, 2008). In the latter case, Kubryakov and Stanichny (2015) found a correlation between  
79 wind curl and the type of eddy formed, they showed that a weakening of large-scale  
80 circulation in response to the decrease of the wind curl leads to the formation of anticyclones  
81 and that an increasing wind curl and circulation induce intensive formation of cyclones. A  
82 constant wind blowing along a regular coast generates coastal upwelling or downwelling  
83 currents, that are known to form surface and subsurface eddies (McGillicuddy, 2014).  
84 Different mechanism have been proposed to explain the observed instabilities and eddy  
85 generation for upwelling systems: adiabatic processes leading to the modification of the  
86 potential vorticity structure of the flow and barotropic/baroclinic instabilities, the effect of  
87 capes or promontories or the planetary beta effect when the coast is oriented along a North-  
88 South direction (see Marchesiello *et al.*, 2003, Morel *et al.*, 2006; Meunier *et al.*, 2010).

89 Although both surface and subsurface intensified eddies can have a signature on  
90 satellite-surface data, in particular on SLA and SST anomaly maps, without additional *in-situ*  
91 measurements, there exists a strong risk that the surface anomalies associated with subsurface  
92 eddies are interpreted as signatures of surface eddies, in particular by data assimilation  
93 systems or, as will be shown in this article, by vertical reconstruction methods based on sea  
94 surface data, such as the surface quasigeostrophy (SQG, see Blumen, 1978; Held *et al.*, 1995;  
95 Isern-Fontanet *et al.*, 2006), or the interior and surface quasigeostrophy (ISQG, see Wang *et*  
96 *al.*, 2013) methods. There exists other methods that could potentially be used to reconstruct  
97 the vertical structures of subsurface vortices, for instance the effective surface

98 quasigeostrophic (ESQG) theory proposed by Lapeyre and Klein (2006; see also Ponte and  
99 Klein, 2013), but they rely on some knowledge or hypothesis of the ocean interior which do  
100 not distinguish surface/subsurface vortices. For instance the ESQG method relies on the  
101 calculation of a single mean vertical profile  $\alpha(z)$  which depends on interior characteristics  
102 (the correlation between the interior potential vorticity anomaly and the stratification). As far  
103 as observations are concerned, a few studies have analyzed the surface signature of subsurface  
104 vortices observed *in-situ* (see for instance, Stammer *et al.*, 1991; Sweeney *et al.*, 2003;  
105 Caballero *et al.*, 2008) and recently Bashmachnikov *et al.* (2013) have shown that two  
106 Meddies, detected at sea, were associated with positive SLA and negative SST anomalies and  
107 suggested that this could be used as a proxy to identify Meddies. Despite these breakthroughs,  
108 we still lack a general theory revealing the exact nature (surface or subsurface) of vortices  
109 from satellite surface observations. The main goal of this study is to propose a simple index,  
110 combining SLA and SST observations, that allows differentiating between surface and  
111 subsurface intensified eddies.

112 The paper is organized as follows. In section 2, we present the quasigeostrophic  
113 framework used in our study and the general inversion problem to reconstruct the vortex  
114 structure. In section 3, we underline the problematic case of distinguishing and inferring the  
115 structure of subsurface vortices. We then define the index that may allow discriminating  
116 between surface and subsurface-intensified eddies from surface observations only (section 4).  
117 The sensitivity of the index to parameters characterising the vortex and its environment is  
118 discussed in section 5. The validation and efficiency of this index is finally tested in section 6  
119 using a regional model simulation of the South Eastern Pacific where surface and subsurface  
120 eddies are found (Chaigneau *et al.*, 2011; Colas *et al.*, 2012). Concluding remarks are  
121 provided in section 7.

## 122 **2. The model**

### 123 **2.1 Quasigeostrophic framework**

124 In order to analyse the physical content of different observed fields, and the possibility to  
125 define some combination in order to infer information on the structure of oceanic eddies, it is  
126 necessary to define equations linking these physical fields. To deal with mesoscale dynamics  
127 and vortices, the simplest equations are the quasi-geostrophic ones which express the  
128 conservation of the quasi-geostrophic potential vorticity (QGPV, see Pedlosky, 1987,  
129 Cushman-Roisin and Beckers, 2011)

$$QGPV = \Delta\psi + \frac{\partial}{\partial z} \left( \frac{f^2}{N^2} \frac{\partial \psi}{\partial z} \right), \quad (1)$$

130 where  $\Delta = \partial_{x^2} + \partial_{y^2}$  is the horizontal Laplace operator,  $f$  is the planetary vorticity or Coriolis  
 131 parameter (here we consider a constant Coriolis parameter  $f = 1.10^{-4} \text{ s}^{-1}$ ),  $\psi$  is the  
 132 streamfunction (proportional to the pressure field  $P = \rho_0 f \psi$ ).  $N$  is the Brunt-Vaisala  
 133 frequency, given by

$$N^2 = \frac{-g \partial_z \bar{\rho}}{\rho_0}, \quad (2)$$

134 where  $g$  is the gravitational acceleration, and  $\bar{\rho}(z)$  is the mean density profile, depending only  
 135 on the vertical coordinate  $z$  and coming from the total stratification expressed as

$$\rho_{tot} = \rho_0 + \bar{\rho}(z) + \rho, \quad (3)$$

136 where  $\rho_0$  is a constant reference density and  $\rho$  is the departure from this reference profile and  
 137 is given by (hydrostatic approximation):

$$\rho = -\frac{1}{g} \frac{\partial P}{\partial z} = -\frac{f \rho_0}{g} \frac{\partial \psi}{\partial z}, \quad (4)$$

138 In the following, we will also consider the sea surface elevation  $\eta$ , or SLA, and the relative  
 139 vorticity  $\zeta$  (used to evaluate the strength of a vortex):

$$\eta = \frac{P(z=0)}{\rho_0 g} = \frac{f}{g} \psi, \quad (5)$$

$$\zeta = \frac{\partial V}{\partial x} - \frac{\partial U}{\partial y} = \nabla^2 \psi, \quad (6)$$

140 Using the previous relationships, the knowledge of potential vorticity allows the calculation  
 141 of all physical fields (see Hoskins *et al.*, 1985; Bishop and Thorpe, 1994) but the boundary  
 142 conditions are strong constraints for this inversion as Eq. 1 is elliptic. Both lateral and vertical  
 143 boundary conditions have thus to be specified to close this so-called Dirichlet-Laplace  
 144 problem and to allow the calculation of the streamfunction and all fields from the knowledge  
 145 of the QGPV. At the vertical boundaries the condition is generally to specify the density  
 146 anomaly which leads to:

$$\left. \frac{\partial \psi}{\partial z} \right|_{z=0} = -\frac{g}{\rho_0 f} \rho(z=0), \quad (7)$$

$$\left. \frac{\partial \psi}{\partial z} \right|_{z=-H} = -\frac{g}{\rho_0 f} \rho(z=-H), \quad (8)$$

148 where  $H$  is the depth of the ocean. As far as horizontal boundaries are concerned, in the  
 149 following, in order to invert potential vorticity and calculate the associated velocity, vorticity  
 150 or stratification, we have assumed periodic horizontal boundary conditions (see Isern-  
 151 Fontanet *et al.*, 2006; Wang *et al.*, 2013). Using Fourier transforms, the QGPV inversion then  
 152 boils down to a 1D (vertical) partial differential equation and can be more easily solved using  
 153 the vertical barotropic and baroclinic modes associated with the stratification (see Wang *et al.*,  
 154 2013).

155

## 156 2.2 General configuration

157 We will consider vortices associated with localized QGPV and surface density anomalies.  
 158 A first important theoretical constraint exists on QGPV and surface/bottom density anomalies.  
 159 Indeed integrating vertically Eq. 1 yields (using 7, 8 and 2):

$$\Delta \bar{\psi} = \overline{QGPV} - \frac{1}{H} \left[ \frac{f\rho(z=0)}{\frac{\partial \rho}{\partial z}(z=0)} - \frac{f\rho(z=-H)}{\frac{\partial \rho}{\partial z}(z=-H)} \right], \quad (9)$$

160 Where  $\bar{\psi}$  and  $\overline{QGPV}$  are the barotropic (vertical average) streamfunction and QGPV. As  
 161 shown in Morel and McWilliams (1997), the vortex is “isolated” if the net horizontal integral  
 162 of the right hand side (potential vorticity and vertical boundary density anomalies) vanishes.  
 163 If this is not the case, the vortex is not isolated and its velocity field decreases as  $1/r$  (where  $r$   
 164 is the distance from its center). Such a slow decrease is not realistic (see Zhang *et al.*, 2013)  
 165 and causes some problems for the inversion in a finite domain. Also notice that its kinetic  
 166 energy would be infinite in an unbounded domain and its sea level anomaly would increase as  
 167  $\log r$ .

168 In order to avoid this and deal with isolated and stable vortices, we have chosen to  
 169 determine a family of vortex structure satisfying the isolation constraint. The QGPV and  
 170 surface density anomalies are thus chosen as follows (see Carton and McWilliams, 1989;  
 171 Herbette *et al.*, 2003):

$$QGPV = Q_0 \left(1 - \left(\frac{r}{R}\right)^2\right) e^{-\left(\frac{r}{R}\right)^2} e^{-\left(\frac{z-z_0}{H_v}\right)^2}, \quad (10)$$

$$\rho(z=0) = \delta\rho_0 \left(1 - \left(\frac{r}{R}\right)^2\right) e^{-\left(\frac{r}{R}\right)^2}, \quad (11)$$

172 where  $r$  is the distance from the vortex center,  $R$  is the vortex radius,  $z$  is the vertical  
 173 coordinate (directed upward and with  $z=0$  at the surface, so that  $z<0$  within the water column)  
 174  $z_0$  is the vertical position of the vortex core and  $H_v$  is its vertical extension. In the following,  
 175 we consider  $R = 50\text{km}$ ,  $H_v = 200\text{m}$ , and the density anomaly at the bottom is considered null,  
 176 but  $Q_0$ ,  $z_0$  and  $\delta\rho_0$  remain variable.

177 Notice the structures given by Eq. 10 and 11 ensure that Eq. 9 is verified, and the vortex is  
 178 thus isolated. As a result, the knowledge of the streamfunction at lateral boundaries becomes  
 179 trivial to invert Eq. 1, periodic boundary conditions and fast Fourier transforms can thus be  
 180 used. Notice in particular that the potential vorticity structure given by Eq. 10 ensures a  
 181 vanishing net QGPV and is constituted of a core surrounded by a crown of opposite sign  
 182 anomaly. Other choices are possible, in particular the vertical superimposition of opposite  
 183 sign PV cores. The latter structure is however baroclinically unstable (see Morel and  
 184 McWilliams, 1997) whereas the chosen family of QGPV structures is generally stable (see  
 185 Carton and McWilliams, 1989; Herbette *et al.*, 2003).

186 Finally, Eq. 1, 7 and 8 are solved using horizontal and vertical discretizations of  
 187  $\Delta x = 5\text{km}$  and  $\Delta z = 10\text{m}$ . The domain will thus be constituted of a square (biperiodic in the  
 188 horizontal) basin of length 500 km and total depth  $H=2000$  m. The background stratification  
 189  $\bar{\rho}(z)$  and  $N^2/f$  are also fixed and given in Fig. 1a. It represents a seasonal thermocline  
 190 located between 100 and 200m with a density jump  $\delta\rho = 1.0/1000$  which separates two weakly  
 191 stratified surface and bottom layers. Figure 1b represents the first second and third baroclinic  
 192 modes associated with this stratification. The first radius of deformation is  $R_1=16$  km.

### 193 **3. The difficult case of subsurface intensified vortices**

194 As surface fields are accessible from spatial observations, and interior fields are more difficult  
 195 to obtain at high resolution, it is tempting to try to reconstruct the vertical structure of eddies  
 196 from the knowledge of surface fields alone. But, if the Dirichlet-Laplace problem, determined  
 197 by Eq. 1, 7,8 and additional lateral boundary conditions, is a well-posed mathematical  
 198 problem, the determination of the streamfunction (and all other physical 3D field) from the  
 199 knowledge of surface boundary fields alone is unfortunately ill-posed. Indeed, notice that,  
 200 given a surface density field, an infinite number of solutions exists with drastically different

201 3D fields, provided different interior QGPV field are chosen. The knowledge of, or some  
 202 hypothesis on, the interior QGPV field are required to determine the 3D structure of a vortex.

203 The “surface quasigeostrophy” approach (SQG, see Blumen, 1978; Held *et al.*, 1995;  
 204 Isern-Fontanet *et al.*, 2006), is based on the assumption of no potential vorticity anomaly  
 205 inside the water column (QGPV =0), so that the dynamics is entirely determined by the  
 206 knowledge of the sea surface density anomalies. As noted by Lapeyre and Klein (2006), this  
 207 hypothesis is generally not well verified and interior PV has to be taken into account too.  
 208 Indeed, as shown in appendix A, the vortex structure reconstructed by the SQG method is  
 209 systematically surface intensified and it is not possible to reconstruct subsurface vortices.

210 Recently Wang *et al.* (2013) proposed to use the knowledge of both the surface density  
 211 and SLA to determine the 3D structure of a vortex. This over-determination of the surface  
 212 boundary condition can indeed lead to some information on the interior QGPV structure and  
 213 improve the calculation of the 3D structure. Their method, called ISQG (interior+surface QG  
 214 method), relies on the combination of the SQG streamfunction  $\psi_{SQG}$  (associated with the  
 215 surface density anomaly alone), and an interior streamfunction  $\psi_i$  (associated with the QGPV,  
 216 see also Lapeyre and Klein, 2006):

$$\psi = \psi_{SQG}(x, y, z) + \psi_i(x, y, z), \quad (12)$$

217 At the surface,  $\psi(x, y, z = 0) = SLA = \psi_{SQG}(x, y, 0) + \psi_i(x, y, 0)$ . Thus, the difference  
 218 between the observed SLA and the surface SQG streamfunction (calculated using the  
 219 observed surface density only) is the signature of the interior QGPV. This proves that the  
 220 surface boundary over-determination indeed allows inferring some information of the 3D  
 221 structure.

222 Despite this promising result, the interior structure is only known at the surface and its  
 223 vertical variation remains unknown. To close the problem, some additional information has to  
 224 be specified and Wang *et al.* (2013) hypothesize that the vertical structure of the interior  
 225 streamfunction (and QGPV) projects on the barotropic and first baroclinic mode only.  
 226 Unfortunately, the latter hypothesis leads to the same problem as the SQG method and the  
 227 vortex structure reconstructed by the ISQG is systematically surface intensified and it is not  
 228 able to identify subsurface vortices (see appendix A). The ESQG theory, proposed by Lapeyre  
 229 and Klein (2006) and extended by Ponte and Klein (2013), can potentially associate surface  
 230 SSH with subsurface structures, but it relies on the knowledge of the interior ocean  
 231 characteristics and is thus not considered here.

232 To conclude, the reconstruction of the 3D structure of vortices from the knowledge of  
 233 surface fields alone is ill-posed and relies on additional hypothesis that, to our knowledge and  
 234 up to now, systematically leads to surface intensified structures. The improvement of the  
 235 existing methods requires being able to reconstruct the structures of both surface and  
 236 subsurface intensified vortices. An indication to determine if the observed surface anomalies  
 237 are associated with a surface or a subsurface intensified structure would thus be an important  
 238 step for such an improvement.

#### 239 **4. Definition of an index to identify surface and subsurface intensified** 240 **eddies**

241 If the complete 3D structure of a vortex seems difficult to calculate precisely from  
 242 surface fields alone, its nature, surface or subsurface, is simpler to determine. Indeed, for  
 243 instance anticyclonic vortices are always associated with a positive sea level anomaly (SLA),  
 244 but the sea surface density anomaly depends on the vertical position of the vortex core: it is  
 245 expected to be negative for surface intensified anticyclones (see Fig. 2a), but positive when  
 246 the vortex core is subsurface, as shown by Bashmachnikov *et al.* (2013) for Meddies. Thus  
 247 the combination of SLA and sea surface density anomaly can lead to the identification of the  
 248 vortex nature.

249 The shape of isopycnal levels for subsurface and surface-intensified eddies is illustrated in  
 250 Fig. 2a. Surface intensified cyclones are associated with a negative SLA and outcropping of  
 251 isopycnals, leading to positive SSp anomalies. In contrast, surface-intensified anticyclones are  
 252 associated with a positive SLA and deepening of isopycnals, leading to a negative SSp. Thus,  
 253 the ratio  $SS\rho / SLA$  is expected to be negative for both surface-intensified cyclones and  
 254 anticyclones. Subsurface-intensified anticyclones still have positive SLA, however the typical  
 255 shape of isopycnal levels is lens-like, with isopycnic levels outcropping the surface  
 256 (McWilliams, 1985; Stammer *et al.*, 1991; McGillicuddy *et al.*, 1999; Sweeney *et al.*, 2003;  
 257 Sánchez and Gil 2004). This results in opposite sign of SSp anomalies in comparison with  
 258 surface intensified vortices and the ratio  $SS\rho / SLA$  is thus positive for both anticyclonic and  
 259 cyclonic subsurface vortices.

260 We thus define:

$$\chi_{\rho} = \frac{SS\rho}{SLA}, \quad (13)$$

261 whose sign can be used to discriminate between surface and subsurface-intensified eddies.

262           The use of  $\chi_\rho$  could be problematic when there exists a homogeneous mixed layer  
 263 topping a subsurface vortex (surface vortices are always characterized by density anomalies).  
 264 However, as shown in Fig. 2b, we expect the signature to be the same for  $\chi_\rho$ . Indeed, for an  
 265 anticyclone, the thermocline will be deformed similarly to the isopycnic levels below. In  
 266 addition, the density anomaly just below the thermocline is also higher above the vortex.  
 267 When mixing occurs, both previous effects contribute to the creation of positive SSp  
 268 anomalies above the vortex core (see Fig. 2b), leading to a positive  $\chi_\rho$ .

269           Finally, as SSp is not directly measured from satellite observations, we also define:

$$\chi_T = \frac{SST}{SLA}, \quad (14)$$

270           At first order, the variations of SSp are dominated by SST variations (except in  
 271 specific regions where salinity can play a substantial role on the stratification: near estuaries,  
 272 region of ice formation/melting, etc...), and SST can be observed remotely. Thus,  $\chi_T$  can also  
 273 be used as an index to distinguish between surface and subsurface-intensified eddies (this will  
 274 be tested and confirmed in section 6.5) except that as temperature and density are  
 275 anticorrelated,  $\chi_\rho$  and  $\chi_T$  are of opposite sign (see Table 1).

276

## 277 5. Sensitivity and errors estimation

278 Qualitative arguments show that the sign of  $\chi_\rho$  can determine the nature of a vortex in  
 279 simple configurations, with monopolar, circular and isolated vortices (here meaning that there  
 280 is no background flow). The latter simplifications are generally not verified in nature and the  
 281 consequence on the validity of our criterion has to be evaluated.

282 We believe that the deformation of vortices (elliptic shapes or inclination of the  
 283 vertical axis) is not problematic: tests have shown that, as long as the vortex remains coherent  
 284 (horizontal deformation below two initial vortex radius), the nature of deformed vortices  
 285 remain correctly detected by the index.

286 When there exists a background flow, the first problem is to identify and calculate the  
 287 part of the SS $\rho$  and SLA signal associated with the vortex and the background flow. A filter  
 288 has to be designed and we have proposed to use a spatial average based on a Gaussian filter  
 289 with a correlation radius  $R_f$  (see appendix B). This filter is used to calculate and remove the  
 290 background flow but is obviously a source of error: it alters the vortex structure and the  
 291 separation between vortex structures and background flow is not obvious if their scales are  
 292 comparable. To evaluate possible errors, we here propose to consider vortices for which the  
 293 streamfunction can be described by a Gaussian structure in the horizontal (Chelton *et al.*,  
 294 2011) and we also assume a localized –again Gaussian- vertical extension:

$$\psi = \psi_{0v} e^{-\frac{r^2}{R^2}} e^{-\frac{(z-z_0)^2}{H_v^2}}, \quad (15)$$

295 Where  $\psi_{0v}$  is the streamfunction maximum,  $R$  is the vortex radius,  $z_0$  is the vertical position of  
 296 the vortex core and  $H_v$  its vertical extent. Notice that, for the sake of simplicity, the vortex  
 297 streamfunction structure is here expressed directly. We could have used Eq. 10-11 but the  
 298 problem would have been more complicated as the background stratification would have  
 299 played a role. Our goal is simply to qualitatively illustrate the possible problems associated  
 300 with the index calculation, so we chose a less realistic but simpler way of specifying the  
 301 vortex. Note that the vortex is still subsurface for  $z_0 < 0$ . We then superimpose a jet-like surface  
 302 current with a streamfunction of the form:

$$\psi = \psi_{0j} \tanh\left(\frac{y-y_0}{L}\right) e^{-\frac{z}{H_j}}, \quad (16)$$

303 where  $L$  is the width of the current,  $H_j$  is its vertical extension and  $y_0$  is the distance between

304 the current and the vortex center. In the following, we consider,  $H_j=200\text{m}$ , but  $\psi^{0j}$ ,  $y_0$ ,  $L$   
 305 remain variable. We also consider a subsurface anticyclonic vortex, with fixed characteristics  
 306 (Gaussian structure defined using Eq. 15): intensity  $\psi_{0v}=7500\text{m}^2\text{s}^{-1}$ , vertical position  $z_0 = -$   
 307  $200\text{m}$ , vertical extension  $H_v=400\text{m}$  and radius  $R=50\text{km}$ . We superimpose both flows and use  
 308 the filter given in appendix B to isolate the vortex flow and calculate  $\chi_p$ . The vortex is  
 309 subsurface, so that we expect  $\chi_p > 0$ .

310 We evaluated the sensitivity of the index calculation to the filter correlation radius  $R_f$   
 311 and jet width  $L$ , the jet intensity and its width, the jet intensity and the position of the jet with  
 312 respect to the eddy center  $y_0$ . The results are shown in Fig. 3. Figure 3a represents the index  
 313 values as a function of the filter correlation radius and jet width. We have chosen  $\psi_{0j} =$   
 314  $\psi_{0v} = 7500\text{m}^2\text{s}^{-1}$  and  $y_0 = +50\text{km}$  (this correspond to the most unfavourable distance as can  
 315 been seen below in Fig. 3c). The  $\chi_p = 0$  isoline is represented so that it is easy to determine  
 316 filter and jet characteristics for which the index calculation is problematic, here associated  
 317 with a negative index which would identify the vortex as surface intensified. When  $R_f$  is  
 318 small, the filter is not active and both structures (jet and vortex SLA and SSp signatures) mix  
 319 so that the evaluation of the vortex nature is problematic, whatever the value of the jet width.  
 320 A minimum filter correlation radius is thus necessary to avoid this problem. Also, as can be  
 321 seen from Fig. 3a, wrong identification is possible when the filter radius is more than 3 time  
 322 the eddy radius and current width being comparable to or less than about 1.3 eddy radius.  
 323 Otherwise, the eddy is always correctly identified as subsurface. This shows that the  
 324 correlation radius of the Gaussian filter has to be chosen so that  $R_f < 3R$ . In addition, we can  
 325 observe that, when the current width and the vortex have the same size ( $L/R=1$ ), the best  
 326 results are obtained when  $R_f \sim R$ .

327 Figure 3b represents the index values as a function of the jet width and jet intensity.  
 328 We thus set the filter radius to  $50\text{km}$  and the distance eddy-jet  $y_0$  to  $+50\text{km}$ . As can be  
 329 expected, background currents influence the calculation of the index and can lead to incorrect  
 330 identification if their characteristics (width and intensity) become comparable to the eddy.  
 331 Also notice that there is no symmetry between eastward ( $\psi_{0j} / \psi_{0v} > 0$ ) and westward current  
 332 ( $\psi_{0j} / \psi_{0v} < 0$ ), this is related to the clockwise rotation of the anticyclonic eddy that has  
 333 accumulative effect on the eastward current and opposite effects when the current is

334 westward. To conclude, close to strong and narrow currents, the detection of the nature of  
335 eddies can be problematic.

336 Fig. 3c represents the index variations as a function of the jet intensity and vortex-  
337 current distance. We have here chosen  $R_f=50$  km and  $L=50$  km. Again, there is no detection  
338 problem when the current is weak enough or when the current is far from the vortex. Notice  
339 that, when the center of the eddy is exactly superimposed with the current ( $y_0=0$ ), the  
340 subsurface eddy is well detected too, because in this particular point the average of the sea  
341 surface height and of the density fields associated with the current are weak. However, for  
342 strong currents (intensity higher than 2.3 times the vortex intensity), and when the vortex  
343 strongly interacts with the current ( $y_0 \sim R$ ), the index does not allow a correct detection of the  
344 vortex nature.

345 To conclude, we have here illustrated that, in a complex environment, when the vortex  
346 is in the vicinity of strong currents, the  $\chi_p$  index can lead to incorrect identification of the  
347 nature (surface or subsurface) of a vortex.

## 348 **6. Validation of $\chi_p$ and $\chi_T$ using a realistic numerical simulation**

### 349 **6.1. Model configuration**

350 In order to examine the general relevance of the proposed indices ( $\chi_p$  and  $\chi_T$ ), we now  
351 use a realistic simulation of the Peru-Chile Current System. In this region, the main  
352 characteristics and dynamics of mesoscale eddies have been recently studied from satellite  
353 data and *in-situ* observations (Chaigneau and Pizarro, 2005a, b; Chaigneau *et al.*, 2008; 2009;  
354 2011; Johnson and McTaggart, 2010; Morales *et al.*, 2012; Stramma *et al.*, 2013). These  
355 studies have revealed the presence of both surface and subsurface intensified eddies that are  
356 preferentially formed near the coast and propagate toward the open ocean. The ROMS  
357 (Regional Ocean Modeling System) is used to reproduce both the observed regional  
358 circulation (Penven *et al.*, 2005; Colas *et al.*, 2008; Montes *et al.*, 2010, 2011; Echevin *et al.*,  
359 2011) where surface and subsurface eddies exist (Colas *et al.*, 2012).

360 ROMS is a free-surface, split-explicit model that solves the hydrostatic primitive  
361 equations based on the Boussinesq approximation (Shchepetkin and McWilliams, 2005;  
362 2009). We used the configuration developed in Colas *et al.* (2012; 2013). The horizontal grid  
363 is isotropic and spans the region between 15°N and 41°S and from 100°W to the South  
364 American coast. The baroclinic Rossby radius of deformation is 50-150 km in the region (*e.g.*

365 Chelton *et al.*, 1998; Chaigneau *et al.*, 2009) and the spatial resolution is  $\sim 7.5$  km, allowing  
 366 to resolve mesoscale structures (Colas *et al.* 2012). 32 stretched terrain-following curvilinear  
 367 vertical coordinates are used. Lateral boundaries are opened and forced by thermodynamical  
 368 fields from the SODA monthly climatology (Carton and Giese, 2008), constructed over the  
 369 1980-2000 period. The model is forced at the surface by heat fluxes from the COADS  
 370 monthly climatology (DaSilva *et al.*, 1994) and by a QuikSCAT monthly climatology for the  
 371 wind-stress (SCOW, Risien and Chelton 2008). As in Colas *et al.* (2012), the simulation was  
 372 performed over a 13 years period, and outputs are 3-day average fields. The first 3 years are  
 373 considered as the spin-up phase and discarded from the stabilized equilibrium solution  
 374 analyzed in this study. The mean currents are realistic and major characteristics of the  
 375 Humboldt Current system are reproduced, but El-Niño events and intra-seasonal variability  
 376 associated with equatorial waves dynamics are not represented due to the climatological  
 377 forcing. In the present study, we first use the last year of the simulation for our analysis.

378 Figure 4 represents the sea surface height and temperature for a given model output  
 379 (1<sup>st</sup> of February of the fourth year of the simulation, that is to say one month after the spin up  
 380 phase), representative of the circulation in the area. Notice the presence of numerous eddies  
 381 but also the larger scale gradients associated with the large scale circulation, and the strong  
 382 coastal upwelling associated with permanent alongshore winds (Colas *et al.*, 2012). Since  
 383 alongshore equatorward wind is the primary forcing of coastal upwelling along an Eastern  
 384 boundary, this upwelling is ubiquitous as indicated by the continuous strip of cold water and  
 385 negative SSH nearshore (Fig. 4). Interested readers are referred to Colas *et al.* (2012; 2013)  
 386 for a more detailed analysis of the simulation.

## 387 **6.2. Analysis of surface and subsurface eddies**

388 The determination of the vortex nature from surface fields is done in 5 steps:

- 389 1. Extract snapshots of the SSH and SS $\rho$ A (or SST) fields from the simulation.
- 390 2. Apply a spatial filter to the latter fields to calculate “anomalies” : SLA, SS $\rho$ A  
 391 and SSTA. The horizontal averaging given in appendix A is used to calculate  
 392 mean fields and the anomalies are the difference between the initial fields and  
 393 the mean fields.
- 394 3. Calculate  $\chi_p = \text{SS}\rho\text{A} / \text{SLA}$  (or  $\chi_T = \text{SSTA} / \text{SLA}$ ). To avoid problems where  
 395  $\text{SLA}=0$ , we calculate  $\chi_p = \text{SS}\rho\text{A} * \text{SLA} / \max(\text{SLA}^2, \epsilon)$ , where  $\epsilon = 10^{-4} \text{ cm}^2$ .

396 4. Identify all vortices: we identify all local SLA extrema for which  $|\text{SLA}| \geq 2\text{cm}$ .  
 397 The extrema are associated with the vortex centers.

398 5. Determine the expected nature of each vortex : we calculate the average value  
 399 of the index near each vortex center (average over 1 grid point). The vortex is  
 400 identified as subsurface intensified if  $\chi_p > 0$  and surface intensified if  $\chi_p < 0$ .

401 Concerning the filtering step, we use a Gaussian filter (see appendix B), and as  
 402 described above the correlation radius  $R_f$  of the filter should be chosen close to the vortex  
 403 radius and smaller than three times the latter. As in this regions the eddy size ranges between  
 404 50 and about 150 km (Chaigneau *et al.*, 2008; 2009), we have thus chosen  $R_f = 150$  km.

405 The anomaly maps (SLA, SSpA and SSTA) corresponding to Fig. 4 are shown in Fig. 5.  
 406 The SLA exhibit positive changes up to 8 cm for anticyclonic eddies and -10 cm for cyclonic  
 407 eddies. The structure of the vortices is well marked (Fig. 5a). The SSpA and SSTA exhibit  
 408 very similar structures, with SSTA variations reaching  $\pm 1^\circ\text{C}$  in the open ocean but as low as -  
 409  $4^\circ\text{C}$  near the coast where the upwelling signal is very strong. The vortex structures are more  
 410 clearly marked on SLA than on SSpA or SSTA maps (see Fig. 5 b and c). Vortex centres are  
 411 thus identified as local extremum on SLA maps. In order to avoid taking into account  
 412 relatively weak eddies, we discarded eddies having a  $|\text{SLA}| < 2$  cm.

413 Figure 6 shows a map of SSpA on which we have superimposed SLA contours. Note  
 414 that both fields, which enter in the calculation of  $\chi_p$ , generally exhibit coherent patterns.  
 415 However, SSpA exhibits a more complex structure, with marked filaments sometimes  
 416 penetrating vortex cores.

417 Figure 7 shows a map of  $\chi_p$ , red areas are associated with positive values,  
 418 corresponding to expected subsurface vortices, blue areas are associated with negative values,  
 419 corresponding to expected surface vortices. We have also superimposed the filtered SLA  
 420 isolines (yellow contours).

421 The expected nature of the vortex, calculated using the index, is then compared to the  
 422 exact nature of the identified vortex is established using the relative vorticity (calculated from  
 423 the total 3D velocity field available from the numerical results). Based on the notion that  
 424 rotation dominates within a vortex, the relative vorticity is indeed a good indicator and can be  
 425 used to detect eddies and to characterize their intensity (McWilliams, 1990). For each  
 426 detected vortex, the depth of maximum absolute relative vorticity  $|Z_{\zeta_{\max}}|$  corresponds to the  
 427 vertical position of the vortex core. Vortices will be considered surface intensified when

428  $|Z_{\zeta_{\max}}|$  is located within the mixed layer (whose thickness is about 30 to 50 m for the present  
429 simulation), and subsurface when it is located below.

430 The four different vortex types were observed: surface anticyclones and cyclones (with  
431 respectively positive and negative relative vorticity reaching their maximum absolute value at  
432 the surface) and subsurface anticyclones and cyclones (with respectively positive and negative  
433 relative vorticity reaching their maximum absolute value inside the water column). Typical  
434 examples are given in Fig. 8 with structures representative of the four possible vortex types  
435 and different amplitudes. The positions of the chosen eddies are indicated on Fig. 7 (denoted  
436 8a-d).

### 437 **6.3. Analysis**

438 For the particular SLA map shown in Fig. 5a, 77 eddies have been identified over the  
439 region. Figure 9 represents the position for all identified eddies superimposed on the SLA  
440 (Fig. 9a) and  $\chi_p$  (Fig. 9b). Crosses (+) are associated with eddies those are correctly identified,  
441 stars (\*) are associated with eddies those are not correctly identified: positive index but  
442 surface intensified core in reality or negative index but subsurface intensified core. Among the  
443 77 eddies detected, 24 (30%) are not correctly identified. As we will see below, this error rate  
444 corresponds to a maximum in the simulation (summer season).

445 There exist two main types of vortices leading to incorrect identification: eddies with a  
446 clear main core and a well-defined structure and eddies having a multicore structure with  
447 superimposed surface and subsurface maxima of relative vorticity.

448 Figure 10 represents the relative vorticity structure of 4 eddies for which the index  
449 yields wrong results. Their positions are indicated in Fig. 7 (denoted 10a, b, c and d) and Fig.  
450 9 (indicated by stars: \*). Vortex 10a is a subsurface anticyclonic vortex identified as a surface  
451 intensified eddy by the index  $\chi_p$  (negative value). Vortex 10b is a surface intensified  
452 anticyclone identified as a subsurface intensified eddy by the index. Notice that most of these  
453 vortices have an index that varies from negative to positive in the vicinity of the center (see  
454 Fig. 9 and 6). Vortices 10c and 10d are different and associated with a multicore structure  
455 (Fig. 10c, d, vertical transects). The strength of both cores is similar so that it seems difficult  
456 to identify the main core.

457 Multicore structures represent a bit more than half the problematic cases. It does not  
458 seem possible to identify multicore vortices without complementary vertical profiles. In  
459 practice any method based on surface observations can thus only reconstruct half the structure

460 (the surface or the subsurface part). Multicore eddies represent a significant fraction in the  
461 present simulation, but many of them can be considered as eddies with a main core (one of the  
462 core is much stronger than the others) and do not cause particular problems. Multicore  
463 structures with cores of similar strength are more problematic. Even though they are rarely  
464 observed in nature (see however Pingree *et al.*, 1993, Tychensky *et al.*, 1998), it is well  
465 known that vortices of the same sign but whose cores are located at different depth tend to  
466 align when they are close to each other (Polvani, 1991; Nof and Dewar, 1994; Correard and  
467 Carton, 1998; Sutyrin *et al.*, 1998; Perrot *et al.*, 2010). It has also been shown that the  
468 interaction of vortices with currents or topography can lead to the formation of secondary  
469 aligned poles for the vortex (Vandermeirsch *et al.*, 2002, Herbette *et al.*, 2003; 2004). The  
470 present results show that they could be more frequent than expected, at least in numerical  
471 simulations, but their identification requires in situ observations.

472 To conclude, the use of the index  $\chi_\rho$  allows us to adequately determine the nature of the  
473 eddy (surface or subsurface) for about 70% of them in this specific output, and among the  
474 incorrect detections about half are associated with vortices that are both surface and  
475 subsurface.

#### 476 **6.4. Statistics over seven years**

477 To evaluate whether the previous results depend on the specific date chosen above, in  
478 particular on seasonal characteristics of the mixed layer (depth, enhanced winter mixing or  
479 summer restratification), the previous calculations have been tested for other dates over the  
480 seven years of simulation. One output corresponding to the 1<sup>st</sup> of each month, have been  
481 selected and analysed. More frequent outputs can be used, but since the vortex evolution is of  
482 the order of a few weeks, one month is an adequate time period to have considerable  
483 evolution of the vortex distribution but still have a good representation of the seasonal  
484 variability. For each selected date, we follow the methods presented in the previous section:  
485 all vortices have been identified, the index  $\chi_\rho$  and the vortex core depth  $Z_{\zeta_{\max}}$  have been  
486 calculated and visually compared with the vertical relative vorticity structure, and multi-core  
487 structures have been identified.

488 The global statistics are presented in Fig. 12, which represents the total number of  
489 vortices detected and the number of wrong identification for the 12 months of the simulation  
490 (mean of seven years and the standard deviation).

491 This graphic shows that the total error varies between 15 to 30% and represents an

492 average of 24%, so that 76% of the vortices are correctly identified.  
493 Multi-core eddies represent 58% of the wrong identification (explaining 14% of the 24%  
494 errors). The error, associated with eddies having a main core, has an average of ~10%, which  
495 is considered good. Interestingly, this error exhibits a seasonal cycle with a minimum in  
496 austral winter and a maximum in late austral summer. This is associated with mixed layer  
497 dynamics. Indeed, during summer, when the mixed layer is shallower, SSTA can be more  
498 influenced by atmospheric forcings than by oceanic processes. In addition, during summer,  
499 the stratification increases and the mixed layer shrinks, reducing the surface signature of  
500 subsurface intensified eddies.

501 To conclude, despite the observed seasonal variability, the errors remain reasonable  
502 and the index is able to correctly identify surface and subsurface vortices during the whole  
503 year.

#### 504 **6.5. Complementary tests with $\chi_T$**

505 As mentioned previously, the sea surface density is not currently observed from space  
506 and only SST is available at an adequate resolution and precision. We have thus evaluated the  
507 use of  $\chi_T$ : Fig. 12 is the same as Fig. 9 but using  $\chi_T$  instead of  $\chi_\rho$ . The results show a very good  
508 general correspondence with  $\chi_\rho$ . In fact, the nature of eddies, as evaluated from  $\chi_T$  and  $\chi_\rho$ ,  
509 differs from 3 to 8% of the vortices and most of the eddies with different  $\chi_T$  and  $\chi_\rho$   
510 identification are in fact multi-core vortices.

511 Also, the rate of success of using  $\chi_T$  is 67% for the general case (and 65% for the  
512 specific output) below but comparable to the rate associated with  $\chi_\rho$ . This shows that in  
513 practice, in this region where salinity does not control the stratification,  $\chi_T$  can be retained  
514 without any drastic loss of –qualitative- information in comparison with  $\chi_\rho$ . Indeed, the  
515 differences between the SST and SSS fields are generally due to large scale variations  
516 (characteristics of surface water masses, influence of precipitation, cloud cover, ...) which is  
517 mostly filtered out within the reference state signal. Regions may however exist where  
518 vortices are constituted of waters with compensating temperature and salinity anomalies, or  
519 region where the mesoscale signal is dominated by salinity variability, such as close to  
520 estuaries. In such cases the use of  $\chi_T$  instead of  $\chi_\rho$  may be more problematic.

## 521 **7. Conclusions: summary, discussion and perspectives**

522 In this work, we have studied the possibility to reconstruct information on the vertical

523 structure of vortices from surface observations. We have first shown that the knowledge of the  
524 interior potential vorticity is crucial to determine the exact 3D structure of a vortex in general.  
525 Theoretical models based on the pure knowledge of instantaneous surface fields yield good  
526 results for surface vortices, but we have shown that subsurface eddies (with an interior  
527 potential vorticity fields intensified in deep layers) cannot be reconstructed by the SQG or  
528 ISQG theory. The ISQG theory improves the results obtained by SQG theory and can be used  
529 for turbulence generated by winds (Rossby waves) where first baroclinic mode and barotropic  
530 mode dominates. But it implicitly hypothesizes that the vortex is surface intensified. ESQG  
531 relies on the knowledge of the ocean interior characteristics, which can be calculated from  
532 ocean circulation models, but projects SSH on a single vertical profile (which can be surface,  
533 subsurface or mixed) for a given area. SQG, ISQG and ESQG approaches have thus to be  
534 handled with care in areas where both surface and subsurface vortices exist.

535 ISQG or ESQG can however be extended to take into account other vertical structures,  
536 determined from climatologies of specific coherent vortices present in oceanic regions for  
537 instance, in particular with subsurface maximum. To do so, a first step is to be able to  
538 determine the nature (surface or subsurface) of a vortex, from surface fields alone.

539 We have thus proposed an index to determine the nature (surface or subsurface) of  
540 vortices using surface anomalies: the ratio of the sea surface density to the sea level  
541 anomalies,  $\chi_p$ . This was tested with data coming from a realistic ocean circulation model in  
542 the Peru-Chile upwelling system and an analysis of tens of vortices.

543 We have shown that there exist wrong identifications associated with different error  
544 sources. First, in realistic configurations, a filter must be applied to determine the part of the  
545 physical fields associated with the vortex signal. We have then shown that the index  
546 calculation can be more difficult in a complex environment: a strong current having  
547 characteristics similar to the vortex can hide the signal of subsurface eddy when it is located  
548 in its vicinity, and lead to errors. We have also shown that multi-core structures, with  
549 subsurface and surface cores of comparable strength, the determination of the position of the  
550 most intense core is difficult, which leads to errors too. This can be problematic in some  
551 regions where deep coherent vortices exist but whose signature can be hidden by vertically  
552 aligned surface eddies.

553 The general rate of success of the method reaches 76% in general, multi-core vortices  
554 representing about half the errors. We have also shown that at first order, the variations of  $SSp$

555 are dominated by SST variations, except in specific regions where salinity can play a  
 556 substantial role on the stratification (near estuaries, region of ice formation/melting, etc.). So  
 557 that the use of the SST anomaly (a field currently available from satellite observations at high  
 558 resolution) is a good proxy for the calculation of the index. We think that our results are  
 559 satisfactory and can be applied to real observations.

560 A problem to be addressed is then the difference in resolution between satellite SST  
 561 and SSH data: the spatial and temporal resolutions of infrared SST observations are, for now,  
 562 far better. This is another potential source of error for the calculation of the index which has to  
 563 be assessed. In the future, wide swath altimetric observations will overcome this bias so that  
 564 the present results will greatly benefit from the breakthrough provided by the SWOT (surface  
 565 water ocean topography satellite, <http://swot.jpl.nasa.gov/>) mission, planned for 2020. Our  
 566 results are thus also contributions to prepare the exploitation of the future SWOT mission for  
 567 the analysis of the dynamics of meso and submesoscale vortices in the ocean. However, for  
 568 present observations, we expect that applications focussing on large scale structures or using  
 569 SST and SSH averaged over several days should limit the problems associated with  
 570 resolution. Testing the proposed method on different surface and subsurface eddies already  
 571 identified by authors or using in situ observations is thus an important perspective of this  
 572 work.

573 The calculation of the index remains very basic and can certainly be improved.  
 574 Different attempts have been made to do so. First, we have tried to use a more quantitative  
 575 approach to identify vortices. Indeed, for surface intensified vortices, calculations (using Eq. 4  
 576 and 5) show that the magnitude of  $SS_{\rho}$  and SLA are linked and should roughly verify:

$$H_v. SS_{\rho}/\rho_o SLA \sim -1, \quad (17)$$

577 Where  $H_v$  is the vertical scale of the surface vortex. For subsurface vortices, this ratio  
 578 should be positive, but weak. We could thus expect that there is a limit of  $\chi_{\rho} < \chi_{\rho}^{\text{lim}}$  beyond  
 579 which the vortex is subsurface, instead of a change of sign. This has been applied with  
 580 success for the main model output analysed in the paper (associated with Fig. 4 to 11): using  
 581  $\chi_{\rho}^{\text{lim}} = 2$  lead to far better results (less than 10% errors). However applying this criterion to the  
 582 general case was disappointing and even lead to degraded general statistics.

583 We have also thought of replacing SLA by the surface relative vorticity, whose field  
 584 seems more closely correlated with SSTA (not shown). In the studied region (southern  
 585 hemisphere and negative  $f$ ) relative vorticity has the same sign as SLA near the vortex center,

586 so that in order to detect surface and subsurface eddies we can use the same algorithms but we  
587 replace SLA by relative vorticity to calculate a new index denoted  $\chi_{\rho}^{\zeta}$ . To identify eddies, the  
588 same method can be used but a new minimum ( $\zeta_{\min} = 0.5 \cdot 10^{-5} \text{ s}^{-1}$ ) has to be defined to remove  
589 weaker eddies. Again the general statistics were not improved in comparison with  $\chi_{\rho}$ . In  
590 addition, relative vorticity is more difficult to calculate using satellite observations, as gridded  
591 altimetric SSH products have a coarse spatial resolution. The relative vorticity field, based on  
592 a double derivative of SSH is then associated with large uncertainties that we believe would  
593 be problematic.

594 Other improvements are possible, such as using an anisotropic filter to better define  
595 the anomalies associated with vortices, or trying to better identify the SST anomaly when it is  
596 not collocated with the vortex center defined by the SLA extrema. Figure 6 indeed shows that  
597 SSpA can be highly variable over the vortex area (delimited by the closed contours of SLA for  
598 instance) so that the calculation of the present index can have strong uncertainties given the  
599 gap between SLA and  $SS_{\rho}$ . We believe an index based on an analysis of the latter fields within  
600 the vortex area could lead to a significant improvement. However, given its simplicity, we  
601 think the present index derived in this first study is useful as a first step.

602 Finally, we have here seen that vortex structures are a complex result of their history.  
603 From their formation to their interaction with large scale background flow, jets or other eddies  
604 (such as alignment with other vortices, as mentioned in this paper), or diabatical  
605 transformations, many processes can modify their structure. Fundamental studies linking all  
606 aspects of vortex evolution to their structure and surface signature are thus of interest too to  
607 improve the proposed index or to determine alternative methods for the determination of the  
608 nature of vortices.

609 Concerning applications, we believe the index yields interesting information to  
610 determine areas where the SQG approach can be used –or not- to calculate a surface velocity  
611 field and where the ISQG method can be generalized to represent subsurface structure,  
612 provided the interior PV structure is projected on new vertical profiles for instance calculated  
613 from local vortex climatologies.

614 The index can also be applied as a proxy to analyze the details of the processes  
615 responsible for the generation and evolution of eddies in nature or in numerical model results,  
616 or to evaluate the contribution of eddies to the general circulation in the ocean, in particular in  
617 regions where water masses are known to subduct or to surface.

618 Finally, a straightforward and obvious application of the index is associated with the  
619 assimilation of SLA or SST anomalies, which are for now, generally associated with surface  
620 intensified eddies. Our work shows that both physical fields are strongly correlated and we  
621 think our results offer the first step of a method to combine them to reconstruct the vertical  
622 structure of a vortex and improve the representation of vortices in realistic models with data  
623 assimilation. Estimating the exact vertical position of the vortex center remains a problem, as  
624 we have shown that the index combines it with the vertical scale of the eddy core and is  
625 probably sensitive to the details of the vortex structure. This has to be studied further but in  
626 general a given oceanic region contains a limited number of coherent vortex types. It thus  
627 seems possible to determine the index characteristics for each vortex type and to connect an  
628 observed anomaly to a single one, then using an average three-dimensional structure of the  
629 latter to project the observed anomalies vertically. This however requires important further  
630 developments.

### 631 **Acknowledgements**

632 This study has benefited from the funding of different projects: EPIGRAM, funded by CNRS  
633 (LEFE/IMAGO) and ANR (grant ANR-08-BLAN-0330-01), “Merging of satellite and *in-situ*  
634 observations for the analysis of meso and submesoscale dynamics”, funded by CNES (OSTST  
635 project), and COMODO, funded by Agence Nationale de la Recherche (ANR-11-MONU-005-  
636 03). We are grateful to Bernard Le Cann (UBO, LPO, Brest) for discussions on vortex studies  
637 and observations. We are also grateful to anonymous referees for their comments that  
638 drastically improved the quality of the manuscript and the calculation of the index.

639

### 640 **Appendix A: evaluation of the SQG and ISQG methods for subsurface** 641 **vortices**

642 As initially shown by Bretherton (1966), building on the idea that the surface density  
643 of the ocean plays the same role as the potential vorticity in the interior of the ocean, several  
644 studies have proposed to compute velocity fields from the knowledge of surface temperature  
645 alone (see Held *et al.*, 1995; Isern-Fontanet *et al.*, 2006), known as the surface quasi-  
646 geostrophy (SQG) theory (Blumen, 1978). It boils down to inverting Eq. 1, 7 and 8,  
647 hypothesizing  $QGPV=0$ . It can be shown that in the Northern hemisphere a positive surface  
648 density anomaly –or a negative temperature anomaly- will in this case be associated via the

649 SQG theory with a surface intensified cyclone. Negative surface density anomaly –or a  
 650 positive temperature anomaly- will be associated by the SQG theory to a surface intensified  
 651 anticyclone (see Isern-Fontan *et al.*, 2006).

652 However, for most oceanic eddies the assumption of no potential vorticity anomaly  
 653 within the water column is not verified, so we can expect some discrepancies between  
 654 reconstructed fields using the SQG method and realistic vortex structures. In particular, the  
 655 difference between the observed sea surface elevation and obtained using SQG and the sea  
 656 surface density anomaly is the signature of the interior QGPV.

657 Based on this idea, Wang *et al* (2013) have proposed an improved method, called ISQG  
 658 (interior+surface QG method), which relies on the addition of an interior streamfunction  $\psi_i$  to  
 659 the SQG streamfunction  $\psi_{SQG}$  associated with the surface density anomaly (Eq. 12,  
 660  $\psi = \psi_{SQG} + \psi_i$ ). The interior streamfunction  $\psi_i$  is then calculated assuming that its vertical  
 661 structure is a combination of the barotropic and first baroclinic modes whose horizontal  
 662 structure is calculated so that the total streamfunction matches the sea surface elevation at the  
 663 surface ( $\psi(z=0) = g\eta/f + \psi_{surf}$ ) and vanishes at the bottom. The solution is given by

$$\psi_i(x, y, z) = \psi_h(x, y)F_1(z) - \psi_{SQG}(x, y, -H) - \psi_h(x, y)F_1(-H), \quad (A1)$$

664

$$\psi_h(x, y) = \frac{1}{F_1(0) - F_1(-H)} [\psi_{surf}(x, y) + \psi_{SQG}(x, y, -H) - \psi_{SQG}(x, y, 0)] \quad (A2)$$

665

666 With this, it can be easily verified that  $\psi(z=0) = \psi_{surf}$  (the sea surface elevation is as  
 667 prescribed),  $\psi(z=-H) = 0$  (the total streamfunction vanishes at the bottom) and

668  $\frac{\partial \psi}{\partial z}(z=0) = \frac{\partial \psi_{SQG}}{\partial z}(z=0)$  (the surface density field is as prescribed). Thus, the ISQG  
 669 method leads to an estimation of interior fields from the sea surface elevation and density  
 670 alone and matching these surface fields.

671 However, the vertical structure of the interior streamfunction, and thus QGPV, is  
 672 empirically determined and only projects on the barotropic mode (which does not vary with  
 673 depth) and first baroclinic mode. If the details of the shape of the first baroclinic mode  
 674 depends on the stratification, it is always intensified at the surface, reaches zero at mid depth

675 or so and reaches another extremum (usually weaker) at the bottom (see Fig. 1b). As a result,  
 676 the vertical structure of the QGPV field associated with the ISQG approach is determined by  
 677 the first baroclinic mode and is always surface intensified.

678 Figure A.1 represents the vorticity, QGPV and density anomaly fields for a chosen  
 679 surface intensified anticyclone with  $\delta\rho_0 = -0.02 \text{ } ^\circ/\text{ }_{00}$ ,  $R= 50 \text{ km}$ ,  $H_v = 200m$ ,  $z_0 = 0m$  and  
 680  $Q_0 = -0.5f$  and its reconstruction using the ISQG and SQG approaches. As demonstrated by  
 681 Wang *et al* (2013) the improvement of the ISQG approach is obvious, in particular for the  
 682 vorticity and density anomaly fields. Notice however that there exist discrepancies in the  
 683 deepest layers for the QGPV field, which exhibits a vertical structure with opposite sign  
 684 anomalies for ISQG, a structure known to be baroclinically unstable. This modification does  
 685 not have a strong impact for the reconstructed fields (at least in the upper layers), but if it was  
 686 used in a predictive model, the evolution and propagation of the (real) QGPV and ISQG  
 687 reconstructed vortices would be different (see Morel and McWilliams, 1997).

688 As the QGPV of the ISQG is surface intensified (and is null for SQG), the  
 689 reconstruction of subsurface eddies thus remains a problem for both SQG and ISQG methods.  
 690 This is illustrated in Fig. A.2 which represents the vorticity, QGPV and density anomaly fields  
 691 for a subsurface vortex with  $\delta\rho_0 = 0. \text{ } ^\circ/\text{ }_{00}$ ,  $R= 50 \text{ km}$ ,  $H_v = 200m$ ,  $z_0 = 300m$  and  
 692  $Q_0 = -0.5f$ . The surface vorticity field remains decently represented, but as expected, the  
 693 QGPV and density fields are this time very different as the structure reconstructed by the  
 694 ISQG method remains surface intensified. These differences get stronger as the vortex core  
 695 vertical position ( $z_0$ ) gets deeper. Also notice that, as the chosen vortex has no density  
 696 signature at the surface ( $\delta\rho_0 = 0. \text{ } ^\circ/\text{ }_{00}$ ) the SQG fields are null.

697 Finally, notice that this time the density field reconstructed by the ISQG method leads  
 698 to opposite sign anomalies: in fact, an anticyclonic vortex with a negative QGPV core has a  
 699 weakly stratified core. As a result, surface intensified anticyclones deflect isopycnic levels  
 700 and the thermocline downward. This is also true for isopycnic levels located below the core of  
 701 subsurface vortices, but the isopycnic levels located above their core are this time pushed  
 702 upward (see for instance Bashmachnikov and Carton, 2012; Bashmachnikov *et al.*, 2014).

703 This has important consequences and accentuates the discrepancies for subsurface  
 704 anticyclones. Indeed, as isopycnic levels located above the core are pushed upward, it is  
 705 reasonable to associate this kind of structure with positive density anomalies at the surface.

706 Figure A.3 represents the velocity, vorticity and potential vorticity fields for a subsurface  
 707 vortex with,  $\delta\rho_0 = 0.0/_{00}$ ,  $R = 50 \text{ km}$ ,  $H_v = 200m$ ,  $z_0 = 300m$  and  $Q_0 = -0.5f$ .

708 The ISQG method leads to subsurface intensified vorticity, but the QGPV field still  
 709 has the same problem and the intensity of the vorticity and density fields are this time much  
 710 weaker than reality. SQG predicts a good thermocline position (density anomaly) but, as a  
 711 positive surface density anomaly is associated with cyclonic vortices, the vorticity has an  
 712 opposite sign.

713 To conclude, both SQG and ISQG have difficulties to represent subsurface eddies.  
 714 Notice that as Eq. 1,7 and 8 are linear, we only considered anticyclonic vortices with a fixed  
 715 QGPV strength ( $Q_0 = -0.5f$ ), but the results are identical for cyclones or anticyclones with  
 716 different strength.

717 The discrepancies associated with the reconstructed ISQG or SQG fields obviously  
 718 depends on several parameters (vortex core depth, radius, shape, ...), but subsurface vortices  
 719 represent a specific problematic category and, despite the recent improvement brought by the  
 720 ISQG approach, the identification and calculation of the 3D fields for this kind of structures  
 721 remains a challenge.

## 722 **Appendix B**

723 Using a low pass filter allows to retain the large scale information within an image while  
 724 reducing the small scale information. Here, the low pass filter  $\bar{\psi}$  of a physical field  $\psi$  is  
 725 calculated using a smoother of the form:

$$\bar{\psi}(i, j) = \frac{\sum_{\Omega_{i,j}} w(i1, j1)\psi(i1, j1)}{\sum_{\Omega_{i,j}} w(i1, j1)}, \quad (\text{B1})$$

726 where the weights  $w$  are defined as:

$$w(i1, j1) = e^{-\frac{(x(i,j)-x(i1,j1))^2+(y(i,j)-y(i1,j1))^2}{R_f^2}}, \quad (\text{B2})$$

727 And  $R_f$  is the correlation radius. The region over which the mean field is calculated is circular  
 728 with a radius  $2 \times R_f$ .

729

730 **References**

- 731 Abraham, E. R., 1998: The generation of plankton patchiness by turbulent stirring. *Nature*,  
732 391 , 577–580.
- 733 Bashmachnikov, I., and X. Carton, 2012: Surface signature of Mediterranean Water eddies  
734 in the North-East Atlantic: effects of upper layer stratification. *Ocean. Sci.*, 8, 931–943.  
735 doi:10.5194/os-8-931-2012.
- 736 Bashmachnikov, I., D. Boutov, and J. Dias, 2013: Manifestation of two meddies in altimetry  
737 and sea-surface Temperature. *Ocean. Sci.*, 9, 249–259.
- 738 Bashmachnikov, I., X. Carton, and T.V. Belonenko, 2014: Characteristics of surface signature  
739 of Mediterranean water eddies. *J. Geophys. Res.*, 119, 10, 7245–7266,  
740 doi: 10.1002/2014JC010244.
- 741 Beron-Vera, F. J., M. J. Olascoaga, and G. J. Goni, 2008: Oceanic mesoscale eddies as  
742 revealed by Lagrangian coherent structures. *Geophys. Res. Lett.*, 35, L12603,  
743 doi:10.1029/2008GL033957.
- 744 Beron-Vera, F. J., María J., Olascoaga, and G. J. Goni, 2010: Surface Ocean Mixing Inferred  
745 from Different Multisatellite Altimetry Measurements. *J. Phys. Oceanogr.*, 40, 2466–2480.
- 746 Bishop, C. H., and A. J. Thorpe, 1994: Potential vorticity and the electrostatics analogy:  
747 Quasi-geostrophic theory. *Q. J. Roy. Meteor. Soc.*, 120, 713–731,  
748 doi: 10.1002/qj.49712051710.
- 749 Blumen, W., 1978 : Uniform potential vorticity flow: Part I. Theory of wave interactions and  
750 two-dimensional turbulence. *J. Atmos. Sci.*, 35, 774–783.
- 751 Bracco, A., S. Clayton, and C. Pasquero, 2009: Horizontal advection, diffusion, and plankton  
752 spectra at the sea surface, *J. Geophys. Res.*, 114, C02001, doi:10.1029/2007JC004671.
- 753 Bretherton, F. P., 1966: Critical layer instability in baroclinic flows. *Q. J. Roy. Meteor. Soc.*,  
754 92,325-334.
- 755 Caballero, A., A. Pascual, G. Dibarboure, and M. Espino, 2008: Sea level and eddy kinetic  
756 energy variability in the Bay of Biscay inferred from satellite altimeter data. *J. Marine. Syst.*,  
757 72, 116-134.
- 758 Calil, P. H. R., Y. L. Jia., R. R. Bidigare, 2008: Eddy activity in the lee of the Hawaiian  
759 Islands. *Deep-Sea Res. Pt.II: Tropical Studies in Oceanography.*, 55, 10-13, 1179-1194,  
760 doi:10.1016/j.dsr2.2008.
- 761 Carton, J. A., and B. S. Giese, 2008: A reanalysis of ocean climate using simple ocean data  
762 assimilation (SODA). *Mon. Wea. Rev.*, 136, 2999-3017, doi:10.1175/2007MWR1978.1.
- 763 Carton, X., and J.C. McWilliams, 1989: Barotropic and baroclinic instabilities of  
764 axisymmetric vortices in a qg model. *Mesoscale/Synoptic Coherent Structures in Geophysical*  
765 *Turbulence*, Elsev. *Oceanogr. ser.*, 225–244.
- 766 Chaigneau, A., and O. Pizarro 2005a: Surface circulation and fronts of the South Pacific  
767 Ocean, east of 120°W, *Geophys. Res. Lett.*, 32, L08605, doi:10.1029/2004GL022070.

- 768 Chaigneau, A., and O. Pizarro, 2005b: Mean surface circulation and mesoscale turbulent flow  
769 characteristics in the eastern South Pacific from satellite tracked drifters, *J. Geophys. Res.*,  
770 110, C05014, doi:10.1029/2004JC002628.
- 771 Chaigneau, A., A. Gizolme, and C. Grados, 2008: Mesoscale eddies off Peru in  
772 altimeter records: Identification algorithms and eddy spatiotemporal patterns, *Prog. Oceanogr.*,  
773 79, 106–119, doi:10.1016/j.pocean.2008.10.013.
- 774 Chaigneau, A., G. Eldin, and B. Dewitte, 2009: Eddy activity in the four major upwelling  
775 Systems from satellite altimetry (1992–2007), *Prog. Oceanogr.*, 83, 117–123,  
776 doi:10.1016/j.pocean.2009.07.012.
- 777 Chaigneau, A., M. Le Texier, G. Eldin, C. Grados, and O. Pizarro, 2011: Vertical structure of  
778 mesoscale eddies in the eastern South Pacific Ocean: A composite analysis from altimetry and  
779 Agro profiling floats. *J. Geophys. Res.*, 116, C11025, doi:10.1029/2011JC007134.
- 780 Chelton, D. B., R. A. deSzoeke, M. G. Schlax, K. El Naggar, and N. Siwertz, 1998:  
781 Geophysical variability of the first baroclinic Rossby radius of deformation. *J. Phys.*  
782 *Oceanogr.*, 28, 433-460.
- 783 Chelton, D. B., M. G. Schlax, R. M. Samelson, and R. A. Szoeke, 2007: Global observations  
784 of large oceanic eddies, *Geophys. Res. Lett.*, 34, L15606, doi:10.1029/2007GL030812.
- 785 Chelton, D. B., and S. P. Xie, 2010: Coupled ocean-atmosphere interaction at oceanic  
786 mesoscales. *Oceanography Magazine.*, 23, 52-69.
- 787 Chelton, D. B., M. G. Schlax, and R. M. Samelson, 2011: Global observations of non linear  
788 mesoscale eddies. *Prog. Oceanogr.*, 91, 167-216.
- 789 Chelton D., 2013: Ocean–atmosphere coupling: Mesoscale eddy effects. *Nature Geosci.*, 6,  
790 594–595 doi:10.1038/ngeo1906.
- 791 Chérubin, L., X. Carton, J. Paillet, Y. Morel and A. Serpette, 2000: Instability of the  
792 Mediterranean Water undercurrents southwest of Portugal: effects of baroclinicity and of  
793 topography. *Oceanol. Acta.*, 23, 551–573.
- 794 Colas, F., X. Capet, J. C. McWilliams, and A. Shchepetkin, 2008: 1997–1998 El Niño off  
795 Peru: A numerical study. *Prog. Oceanogr.*, 79 (2), 138-155.
- 796 Colas, F., J. C. McWilliams, X. Capet, and J. Kurian, 2012: Heat balance and eddies in the  
797 Peru-Chile current system. *Climate Dynamics.*, 39, 509-529. doi:10.1007/s00382-011-1170-6.
- 798 Colas, F., X. Capet, J. C. McWilliams, and Z. Li, 2013: Mesoscale eddy buoyancy flux and  
799 eddy-induced circulation in Eastern Boundary Currents. *J. Phys. Oceanogr.*, 43, 1073-1095.
- 800 Correard, S., and X. Carton, 1998: Vertical alignment of geostrophic vortices: on the influence  
801 of the initial distribution of potential vorticity. *Proceedings of the IUTAM Symposium on*  
802 *Simulation and identification of organized structures in flows.* Kluwer Acad. Publ., 52, 191-  
803 200.
- 804 Cushman-Roisin, B., and Beckers J-M, 2011: *Introduction to Geophysical Fluid Dynamics.*  
805 2nd Edition. Academic Press, 875 pp.

- 806 d'Ovidio, F., V. Fernandez, E. Hernandez-Garcia, and C. Lopez, 2004: Mixing structures in  
807 the Mediterranean sea from finite size Lyapunov exponents. *Geophys. Res. Lett.*, 31, L17203.
- 808 DaSilva, A., A. C. Young, and S. Levitus, 1994: "Atlas of surface marine data 1994, volume 1.  
809 Algorithms and procedures.," Tech. Rep. 6, U.S. Department of Commerce, NOAA, NESDIS.
- 810 Echevin, V., F. Colas, A. Chaigneau, and P. Penven, 2011: Sensitivity of the Northern  
811 Humboldt Current System nearshore modeled circulation to initial and boundary conditions.  
812 *J. Geophys. Res.*, 116, C07002, doi:10.1029/2010JC006684.
- 813 Frenger, I., N. Gruber, R. Knutti, and M. Münnich, 2013: Imprint of Southern Ocean eddies  
814 on winds clouds and rainfall. *Nature Geosci.*, 6, 608-612, doi:10.1038/ngeo1863.
- 815 Garfield, N., C. A. Collins, R. G. Paquette, and E. Carter, 1999: Lagrangian exploration of the  
816 California Undercurrent. *J. Phys. Oceanogr.*, 29, 560–583.
- 817 Held, I. M., R. T. Pierrehumbert, S. T. Garner, and K. L. Swanson, 1995: Surface quasi-  
818 geostrophic dynamics. *J. Fluid. Mech.*, 282, 1-20.
- 819 Herbette, S., Y. Morel, and M. Arhan, 2003: Erosion of a surface vortex by a seamount. *J.*  
820 *Phys. Oceanogr.*, 33, 1664–1679.
- 821 Herbette, S., Y. Morel, and M. Arhan, 2004: Subduction of a surface vortex under an  
822 outcropping front. *J. Phys. Oceanogr.*, 34, 1610–1627. doi:10.1175/1520-  
823 0485(2004)034<1610:SOASVU>2.0.CO;2.
- 824 Hoskins, B. J., M. E. McIntyre, and A. W. Robertson, 1985: On the use and significance of  
825 isentropic potential vorticity maps. *Q. J. Roy. Meteor. Soc.*, 111, 877-946.
- 826 Isern-Fontanet, J., B. Chapron, G. Lapeyre, and P. Klein, 2006: Potential use of microwave  
827 sea surface temperatures for the estimation of ocean currents. *Geophys. Res. Lett.*, 33, 1-5,  
828 L24608, doi:10.1029/2006GL027801.
- 829 Jayne, S. R., and J. Marotzke, 2002: The oceanic eddy heat transport. *J. Phys. Oceanogr.*, 32,  
830 3328– 3345.
- 831 Johnson, G. C., and K. E. McTaggart, 2010: Equatorial Pacific 13°C water eddies in the  
832 eastern subtropical South Pacific Ocean. *J. Phys. Oceanogr.*, 40, 226-236,  
833 doi:10.1175/2009JPO42871.
- 834 Kubryakov, A. A., and S. V. Stanichny, 2015: Seasonal and interannual variability of the Black  
835 Sea eddies and its dependence on characteristics of the large-scale circulation. *Deep-Sea. Res.*  
836 *Pt. I.*, 97, 80-91, doi:10.1016/j.dsr.2014.12.002
- 837 Lapeyre, G., and P. Klein, 2006: Dynamics of the upper oceanic layers in terms of surface  
838 quasigeostrophy theory. *J. Phys. Oceanogr.*, 36, 165-176. Lévy, M., and P. Klein, 2004: Does  
839 the low frequency variability of mesoscale dynamics explain a part of the phytoplankton and  
840 zooplankton spectral variability? *P. Roy. Irish. ACAD. A.*, 460, 1673-1683, doi:  
841 10.1098/rspa.2003.1219.
- 842 Marchesiello, P., J.C. McWilliams, and A. Shchepetkin, 2003: Equilibrium structure and  
843 dynamics of the California current system. *J. Phys. Oceanogr.*, 33, 753–783.

- 844 Martin, A. P., and K. J. Richards, 2001: Mechanisms for vertical transport within a North  
845 Atlantic mesoscale eddy. *Deep-Sea. Res. Pt. II.*, 48, 757–773.
- 846 McGillicuddy, D. J., and A.R. Robinson, 1997: Eddy induced nutrient supply and new  
847 production in the Sargasso Sea. *Deep-Sea. Res. Pt. I.*, 44(8), 1427-1450.
- 848 McGillicuddy, D. J., R. Johnson, D. A. Siegel, A. F. Michaels, N. R. Bates, and A. H.  
849 Knap, 1999: Mesoscale variations in biogeochemical properties in the Sargasso Sea. *J.*  
850 *Geophys. Res.*, 104(C6), c13381-13394.
- 851 McGillicuddy, D. J., 2014: Formation of Intrathermocline Lenses by Eddy–Wind Interaction.  
852 *J. Phys. Oceanogr.*, 45, 606-612, doi: 10.1175/JPO-D-14-0221.1.
- 853 McWilliams, J.C., 1985: Submesoscale, coherent vortices in the ocean.  
854 *Rev. Geophys.*, 23, 165-182.
- 855 McWilliams, J.C., 1990: The vortices of two-dimensional turbulence. *J. Fluid Mech.*, 219,  
856 361–385.
- 857 Meunier, T., V. Rossi, Y. Morel, and X. Carton, 2010: Influence of bottom topography on an  
858 upwelling current: Generation of long trapped filaments. *Ocean. Model.*, 35, 277–303,  
859 doi:10.1016/j.ocemod.2010.08.004
- 860 Montes, I., F. Colas, X. Capet, and W. Schneider, 2010: On the pathways of the equatorial  
861 subsurface currents in the eastern equatorial Pacific and their contributions to the Peru-Chile  
862 undercurrent. *J. Geophys. Res.*, 115, C09003, doi:10.1029/2009JC005710.
- 863 Montes, I., W. Schneider, F. Colas, B. Blanke, and V. Echevin, 2011: Subsurface connections  
864 in the eastern tropical Pacific during La Niña 1999–2001 and El Niño 2002–2003. *J. Geophys.*  
865 *Res.*, 116, C12022, doi:10.1029/2011JC007624.
- 866 Morales, C. E., S. Hormazabal, M. Correa-Ramirez, O. Pizarro, N. Silva, C. Fernandez, V.  
867 Anabalón, and M. L. Torreblanco, 2012: Mesoscale variability and nutrient-phytoplankton  
868 distribution off central-southern Chile during the upwelling season: the influence of  
869 mesoscale eddies. *Prog. Oceanogr.*, 104, 17–29.
- 870 Morel, Y., and J.C. McWilliams, 1997: Evolution of isolated interior vortices in the ocean. *J.*  
871 *Phys. Oceanogr.*, 27, 727-748.
- 872 Morel, Y., and J.C. McWilliams, 2001: Effects of isopycnal and diapycnal mixing on  
873 the stability of oceanic currents. *J. Phys. Oceanogr.*, 31, 2280-2296.
- 874 Morrow, R., and P. Y. LeTraon, 2012: Recent advances in observing mesoscale  
875 ocean dynamics with satellite altimetry. *Adv. Space. Res.*, 50, 1062–1076.
- 876 Munk, W. H., and C. Wunsch, 1998: Abyssal recipes II: Energetics of tidal and wind mixing.  
877 *Deep-Sea. Res. Pt. I.*, 45, 1977–2010.
- 878 Nof, D., and W. K. Dewar, 1994: Alignment of lenses: laboratory and numerical experiments.  
879 *Deep-Sea. Res. Pt. I.*, 41, 1207-1229.
- 880 Paillet, J., B. Le Cann, A. Serpette, Y. Morel, and X. Carton, 2002: Dynamics and evolution  
881 of a Northern Meddy. *J. Phys. Oceanogr.*, 32, 55-79.

- 882 Pasquero, C., A. Bracco, and A. Provenzale, 2005: Impact of the spatiotemporal variability of  
883 the nutrient flux on primary productivity in the ocean. *J. Geophys. Res.*, 110, C07005 doi:  
884 10.1029/2004JC002738.
- 885 Pedlosky, J., 1987: *Geophysical Fluid Dynamics.*, New York, Springer-Verlag, 710 pp.
- 886 Penven, P., V. Echevin, J. Pasopera, F. Colas, and J. Tam, 2005: Average circulation, seasonal  
887 cycle, and mesoscale dynamics of the Peru Current System: A modeling approach. *J.*  
888 *Geophys. Res.*, 110, C10021, doi:10.1029/2005JC002945
- 889 Perrot, X., X. Carton, and A. Guillou, 2010: Geostrophic vortex alignment in external shear or  
890 strain. *Proceedings of the Symposium on Turbulence in the Atmosphere and Oceans*, IUTAM  
891 book series 28, Springer, 217-224.
- 892 Pingree, R.D., and B. Le Cann, 1992a: Three anticyclonic Slope Water Oceanic eDDIES  
893 (SWODDIES) in the southern Bay of Biscay in 1990. *Deep-Sea. Res.*, 39 (7/8), 1147–1175.
- 894 Pingree, R. D., and B. Le Cann, 1992b: Anticyclonic eddy X91 in the southern Bay of  
895 Biscay, may 1991 to February 1992. *J. Geophys. Res.*, 97, doi:10.1029/92JC01181.
- 896 Pingree, R. D., and B. Le Cann, 1993: Structure of a Meddy (Bobby 92) southeast of the  
897 Azores. *Deep Sea Research* 40(10), 2077-2103, doi:10.1016/0967-0637(93)90046-6.
- 898 Polvani, L. M., 1991: Two-layer geostrophic vortex dynamics. Part 2. Alignment and two-  
899 layer V-states. *J. Fluid. Mech.*, 225, 241–270.
- 900 Ponte, A.L. and P. Klein, 2013: Reconstruction of the upper ocean 3D dynamics from high  
901 resolution sea surface height. *Ocean Dynamics*, 63, 777-791.
- 902 Risien, C. M., and D.B. Chelton, 2008: A global climatology of surface wind and wind stress  
903 fields from eight years of QuikSCAT scatter-ometer data. *J. Phys. Oceanogr.*, 38, 2379–  
904 2413. doi:10.1175/2008.JPO3881.1.
- 905 Sánchez, R., and J. Gil, 2004: 3D structure, mesoscale interactions and potential vorticity  
906 conservation in a swoddy in the Bay of Biscay. *J. Marine. Syst.*, 46, 47–68.
- 907 Shchepetkin, A. F., and J. C. McWilliams, 2005: The regional ocean modeling  
908 system (ROMS): a split-explicit, free surface, topography following coordinates ocean  
909 model. *Ocean. Model.*, 9, 347-404.
- 910 Shchepetkin, A. F., and J. C. McWilliams, 2009: Correction and Commentary for "Ocean  
911 forecasting in terrain-following coordinates: formulation and skill assessment of the Regional  
912 Ocean Modeling System" by Haidvogel et al.. *J. Computat. Phys.*, 227, 3595-3624.
- 913 Stammer, D., H.-H. Hinrichsen, and R. H. Käse, 1991: Can meddies be detected by satellite  
914 altimetry? *J. Geophys. Res.*, 96(C4), 7005–7014, doi:10.1029/90JC02740.
- 915 Stramma, L. H., W. Bange, R. Czeschel, A. Lorenzo, and M. Frank, 2013: On the role of  
916 mesoscale eddies for the biological productivity and biogeochemistry in the eastern tropical  
917 Pacific Ocean off Peru. *Biogeosci. Discuss.*, 10, 9179-9211, doi:10.5194/bgd-10-9179-2013.
- 918 Sutyrin G. G., J. C. McWilliams, R. Saravanan, 1998: Co-rotating stationary states and vertical  
919 alignment of geostrophic vortices with thin cores. *J. Fluid. Mech.*, 357, 321-349.

- 920 Sweeney, E. N., D. J. McGillicuddy, K. O. Buesseler, 2003: Biogeochemical impacts due to  
921 mesoscale eddy activity in the Sargasso Sea as measured at the Bermuda Atlantic Time-series.  
922 Deep-Sea. Res. Pt. II., 50, 3017-3039.
- 923 Thompson, A. F., 2008: The atmospheric ocean: eddies and jets in the Antarctic Circumpolar  
924 Current. *Philos. T. Roy. Soc. A.*, 366, 4529–4541.
- 925 Treguier, A. M., J. Deshayes, C. Lique, R. Dussin, and J. M. Molines., 2012: Eddy  
926 contributions to the meridional transport of salt in the North Atlantic. *J. Geophys. Res.*, 117,  
927 C05010, doi:10.1029/2012JC007927.
- 928 Tychensky, A., and X. Carton, 1998: Hydrological and dynamical characterization of meddies  
929 in the Azores region: A paradigm for baroclinic vortex dynamics. *J. Geophys.*  
930 *Res.*, 103, 25061–25079.
- 931 Vandermeirsch, F., Y. Morel, and G. Sutyrin, 2002: Resistance of a coherent vortex to a  
932 vertical shear. *J. Phys. Oceanogr.*, 32, 3089-3100.
- 933 Wang, J., G.R. Flierl, J.H. LaCasce, J.L. McClean, A. Mahadevan, 2013: Reconstructing the  
934 Ocean's Interior from Surface Data. *J. Phys. Oceanogr.*, 43, 1611–1626.
- 935 Wunsch, C., 1999: Where do ocean eddy heat fluxes matter? *J. Geophys. Res.*, 104, 13,235–  
936 13,249.
- 937 Wunsch, C., and R. Ferrari, 2004: Vertical mixing, energy, and the general circulation of the  
938 oceans. *Annu. Rev. Fluid Mech.*, 36, 281-314.
- 939 Zhang, Z., Y. Zhang, W. Wang, and R. X. Huang, 2013: Universal structure of mesoscale  
940 eddies in the ocean. *Geophys. Res. Letter.*, 40, 3677-3681.
- 941

942 **Tables**

943 Table 1: Sign of indices and SLA for the different vortex types.

| $\chi_\rho = \frac{SS\rho}{SLA}$ | $\chi_T = \frac{SST}{SLA}$ | SLA | Nature of the vortex        |
|----------------------------------|----------------------------|-----|-----------------------------|
| > 0                              | < 0                        | > 0 | Subsurface and anticyclonic |
| > 0                              | < 0                        | < 0 | Subsurface and cyclonic     |
| < 0                              | > 0                        | > 0 | Surface and anticyclonic    |
| < 0                              | > 0                        | < 0 | Surface and cyclonic        |

944

945 **Figures captions**

946 Fig. 1: Chosen density profile  $\bar{\rho}(z)$  and stratification (panel a) and vertical structure of the  
 947 first three baroclinic modes (panel b).

948 Fig. 2: Isopycnal displacements, SLA and SST anomaly for: a) the four different eddies types.  
 949 b) a subsurface eddy with a mixed layer.

950 Fig. 3: Sensitivity study of the index to: a) the filter radius and the current width, b) the jet  
 951 intensity and its width, c) the jet intensity and the distance jet-eddy.

952 Fig. 4: SSH in m (a) and SST in °C (b) over the Peru-Chile domain on February (1<sup>st</sup>) of the  
 953 last year (7<sup>th</sup>) of the climatological simulation.

954 Fig. 5: SLA in m (a), SSTA in °C (b) and SSpA in kg.m<sup>-3</sup> (c), where the “anomalies” are  
 955 calculated from the total fields presented in Fig. 4.

956 Fig. 6: SSpA in kg.m<sup>-3</sup> superimposed on the SLA (black lines).

957 Fig. 7: Map of the index  $\chi_\rho$  (red for positive index and subsurface vortices, blue for negative  
 958 index and surface vortices) superimposed on the SLA (red lines) in the Peru-Chile area  
 959 calculated from the fields presented in Fig. 5 (the position of specific eddies analysed in this  
 960 study is indicated by numbers).

961 Fig. 8: Relative vorticity (East-West and North-South transects, vertical profile) of eddies  
 962 correctly identified : a- cyclonic surface eddy, b- anticyclonic surface eddy, c- cyclonic  
 963 subsurface eddy, d- anticyclonic subsurface eddy. The position of each vortex (denoted 8a, b, c  
 964 and d) is indicated in Fig. 7.

965 Fig. 9: SLA (left panel, same as Fig. 5a but with fewer contours) and Index  $\chi_\rho$  (right panel,  
 966 same as Fig. 7). Eddies that are correctly identified by the index are labelled with crosses (+).  
 967 Eddies that are not correctly identified by the index are labelled with stars (\*).

968 Fig.10: Vorticity structure of the 4 eddies which the index yields wrong results. For each  
 969 vortex, we have represented the East-West and North-South transects of relative vorticity, and  
 970 a mean vertical profile near the center. The positions of each vortex (denoted 10a, b, c and d)  
 971 are also given on Fig.7.

972 Fig. 11: Diagram representing the monthly statistics of vortices identification for the  
 973 numerical simulation used in the study (the black intervals represent the standard deviation  
 974 for each month over the seven years of simulation).

975 Fig. 12: Same as Fig. 9 but using  $\chi_T$  instead of  $\chi_\rho$ . Eddies that are correctly identified by the  
 976 index are labelled with crosses (+). Eddies that are not correctly identified by the index are  
 977 labelled with stars (\*).

978 Fig.A.1: Vertical section of vorticity, QGPV and density fields for a surface anticyclone with  
 979  $\delta\rho_0 = -0.02 \text{ } ^0/_{00}$ ,  $R= 50 \text{ km}$ ,  $H_v = 200m$ ,  $z_0 = 0m$  and  $Q_0 = -0.5f$  (left column) and  
 980 reconstructed fields for ISQG (middle column) and SQG (right column).

981 Fig. A.2: Vorticity, QGPV and density fields for a surface anticyclone with  $\delta\rho_0 = 0. \text{ } ^0/_{00}$ ,  $R=$   
 982  $50 \text{ km}$ ,  $H_v = 200m$ ,  $z_0 = 300m$  and  $Q_0 = -0.5f$  (left column) and reconstructed fields for  
 983 ISQG (middle column) and SQG (right column).

984 Fig. A.3: Vorticity, QGPV and density fields for a surface anticyclone with  $\delta\rho_0 = 0.02 \text{ } ^0/_{00}$ ,  
 985  $R= 50 \text{ km}$ ,  $H_v = 200m$ ,  $z_0 = 300m$  and  $Q_0 = -0.5f$  (left column) and reconstructed fields  
 986 for ISQG (middle column) and SQG (right column).

987

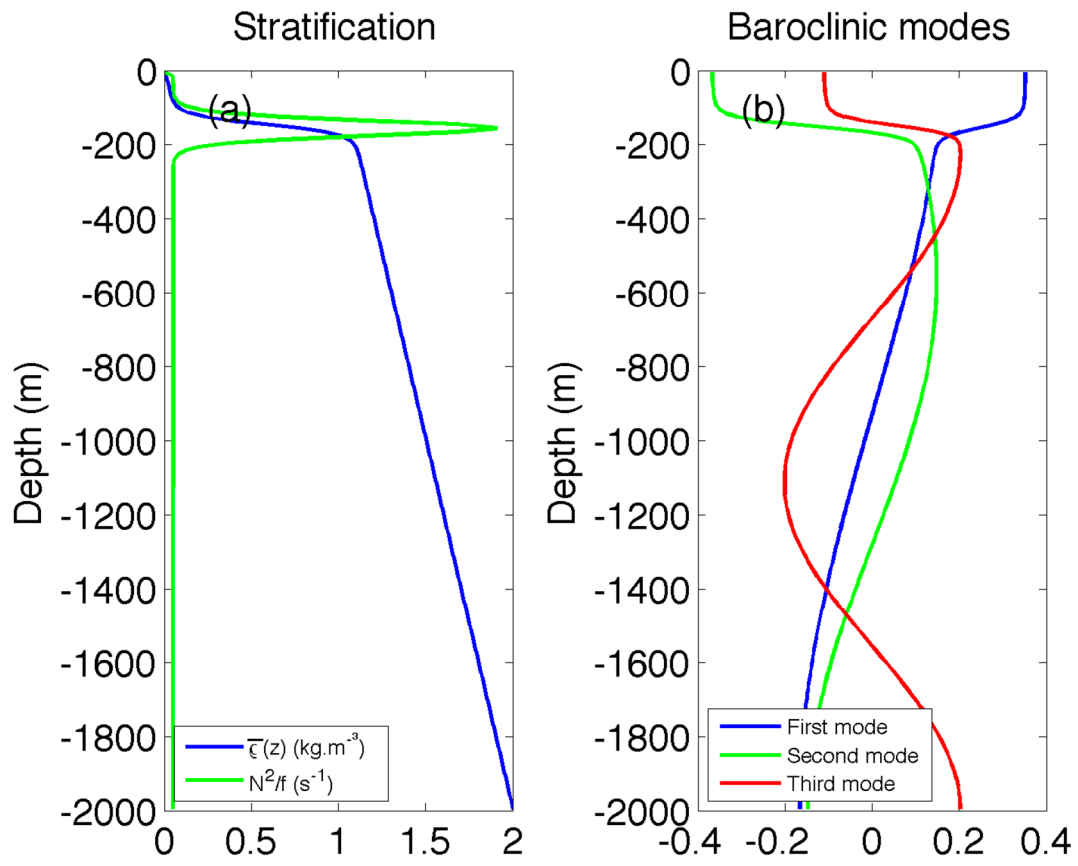


Fig. 1: Chosen density profile  $\bar{\rho}(z)$  and stratification (panel a) and vertical structure of the first three baroclinic modes (panel b).

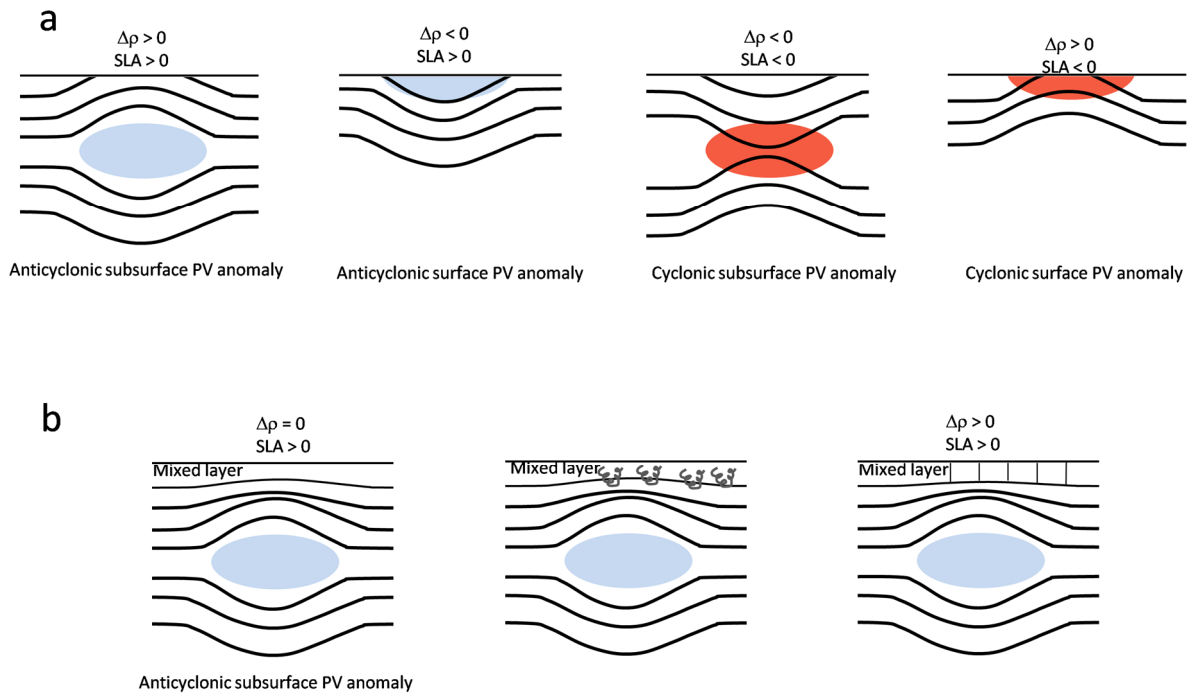
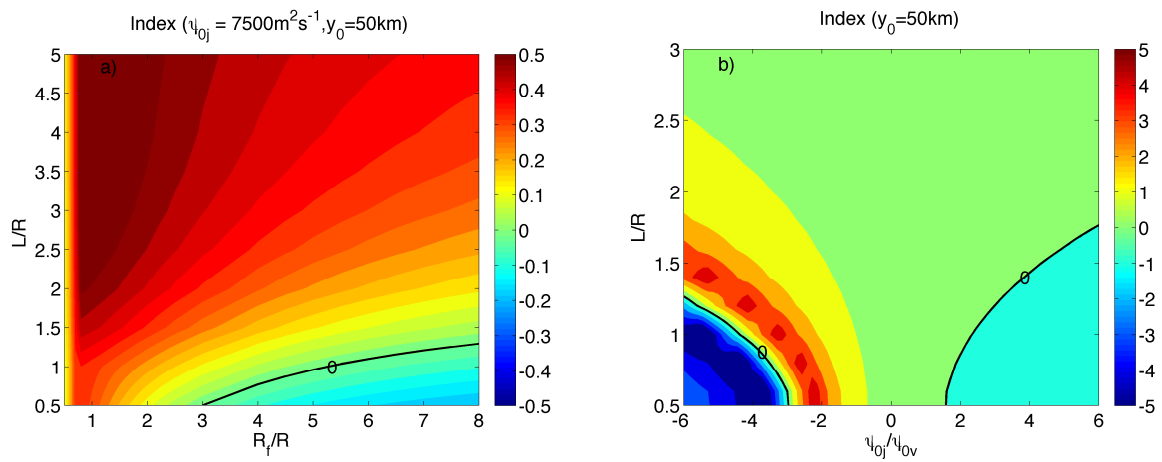


Fig. 2: Isopycnal displacements, SLA and SST anomaly for: a) the four different eddies types. b) a subsurface eddy with a mixed layer.

990



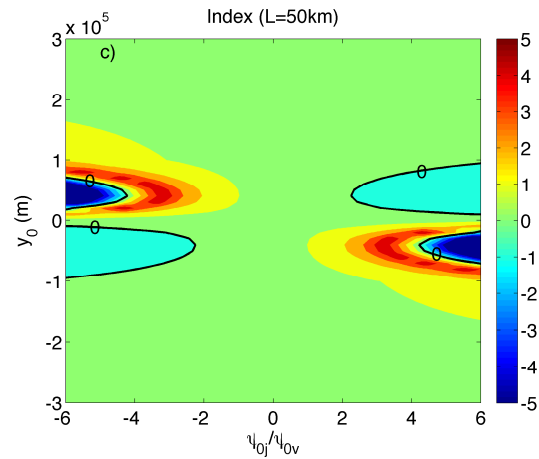


Fig. 3: Sensitivity study of the index to: a) the filter radius and the current width, b) the jet intensity and its width, c) the jet intensity and the distance jet-eddy.

991

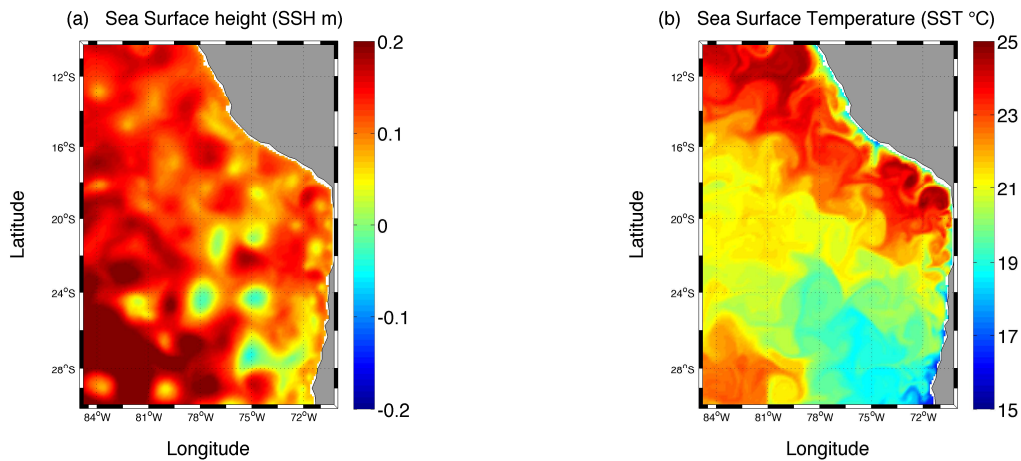


Fig. 4: SSH in m (a) and SST in  $^{\circ}\text{C}$  (b) over the Peru-Chile domain on February (1<sup>st</sup>) of the last year (7<sup>th</sup>) of the climatological simulation.

992

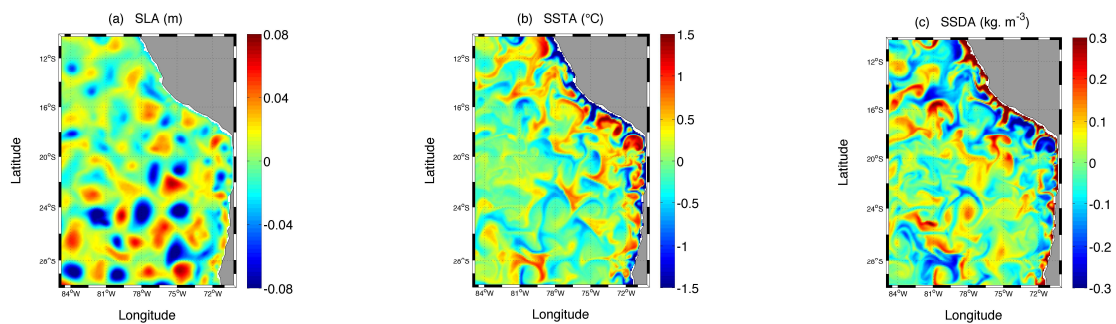


Fig. 5: SLA in m (a), SSTA in  $^{\circ}\text{C}$  (b) and SSpA in  $\text{kg}\cdot\text{m}^{-3}$  (c), where the “anomalies” are calculated from the total fields presented in Fig. 4.

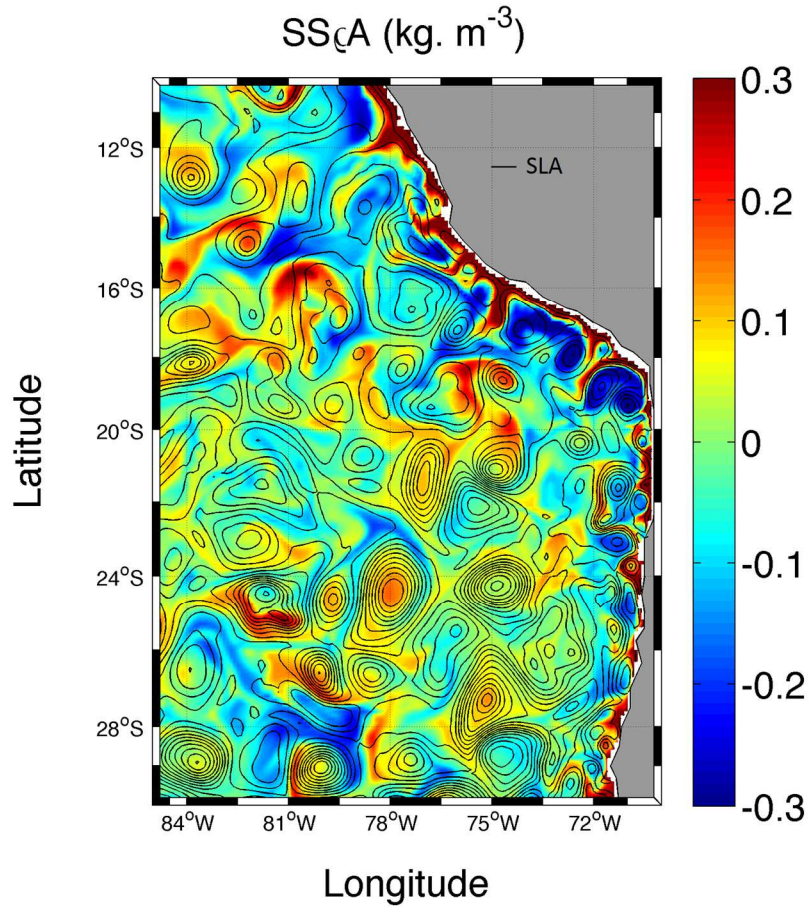


Fig. 6:  $SS_{cA}$  in  $\text{kg. m}^{-3}$  superimposed on the SLA (black lines)

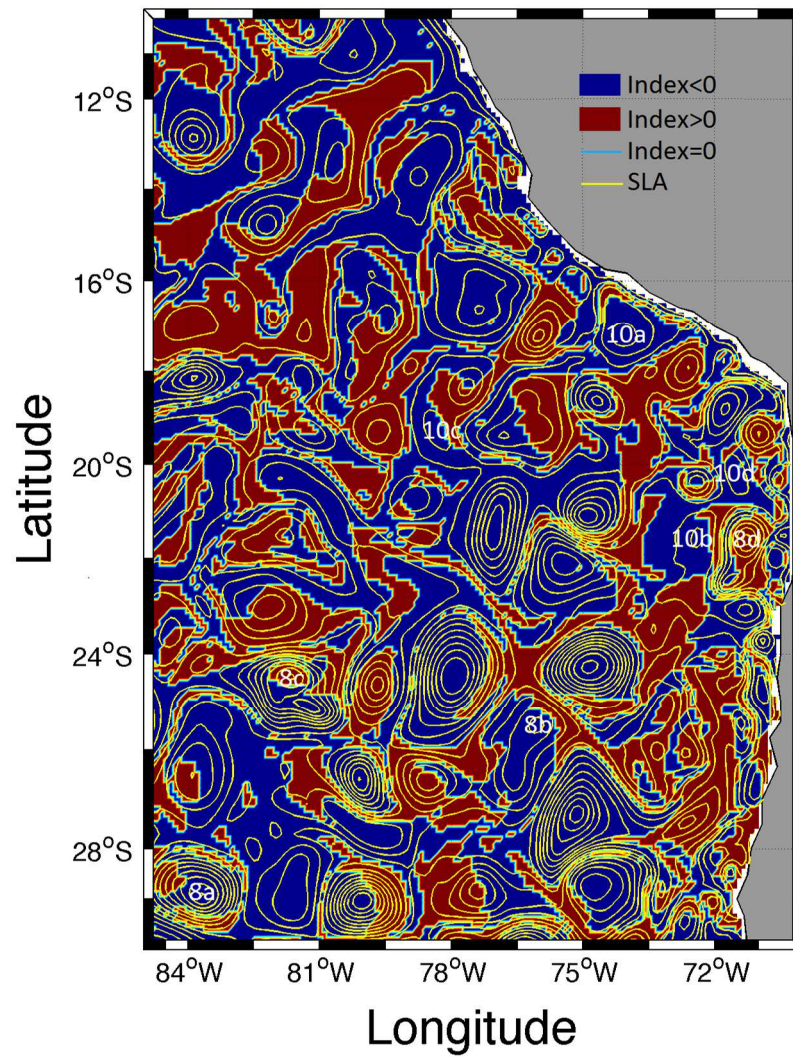
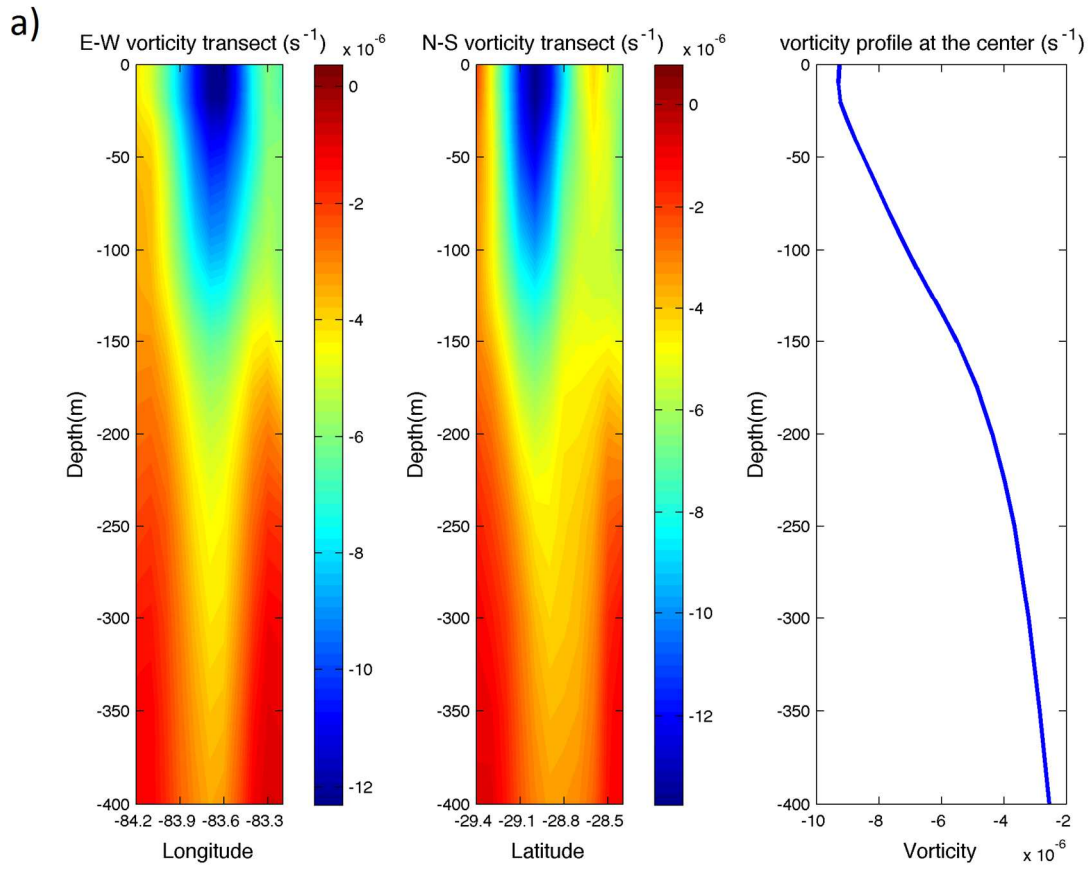
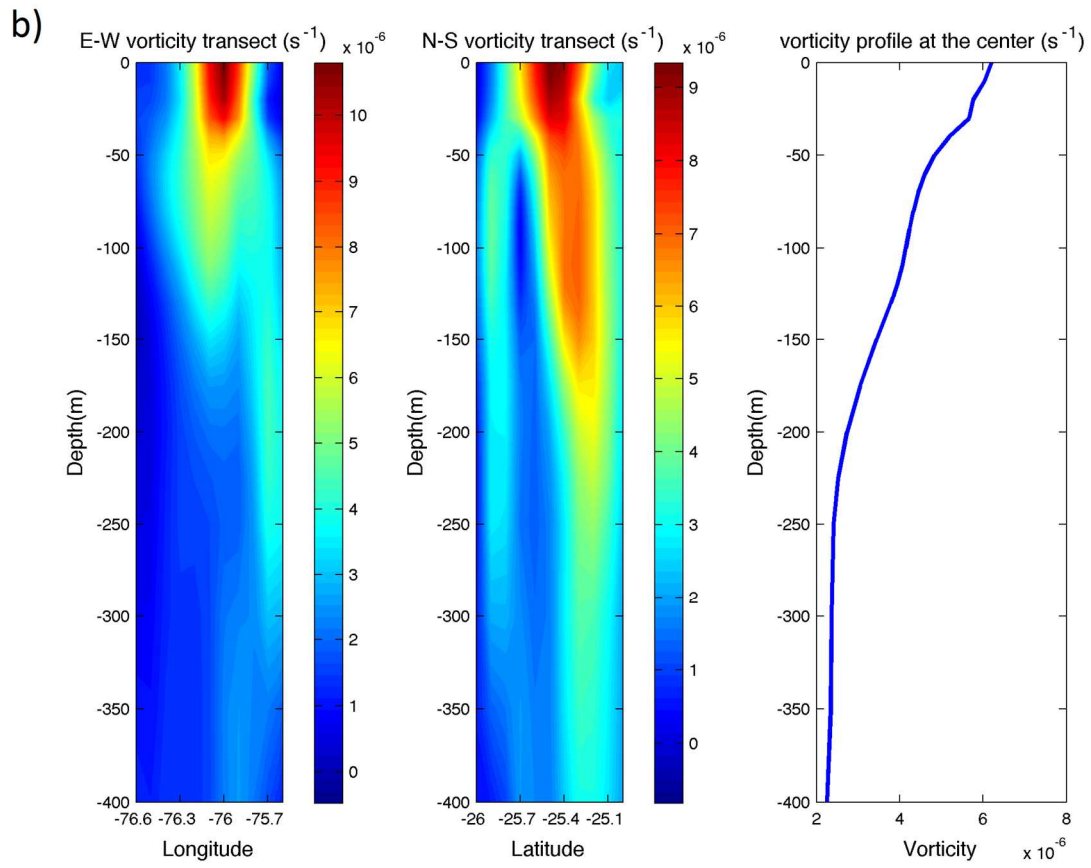
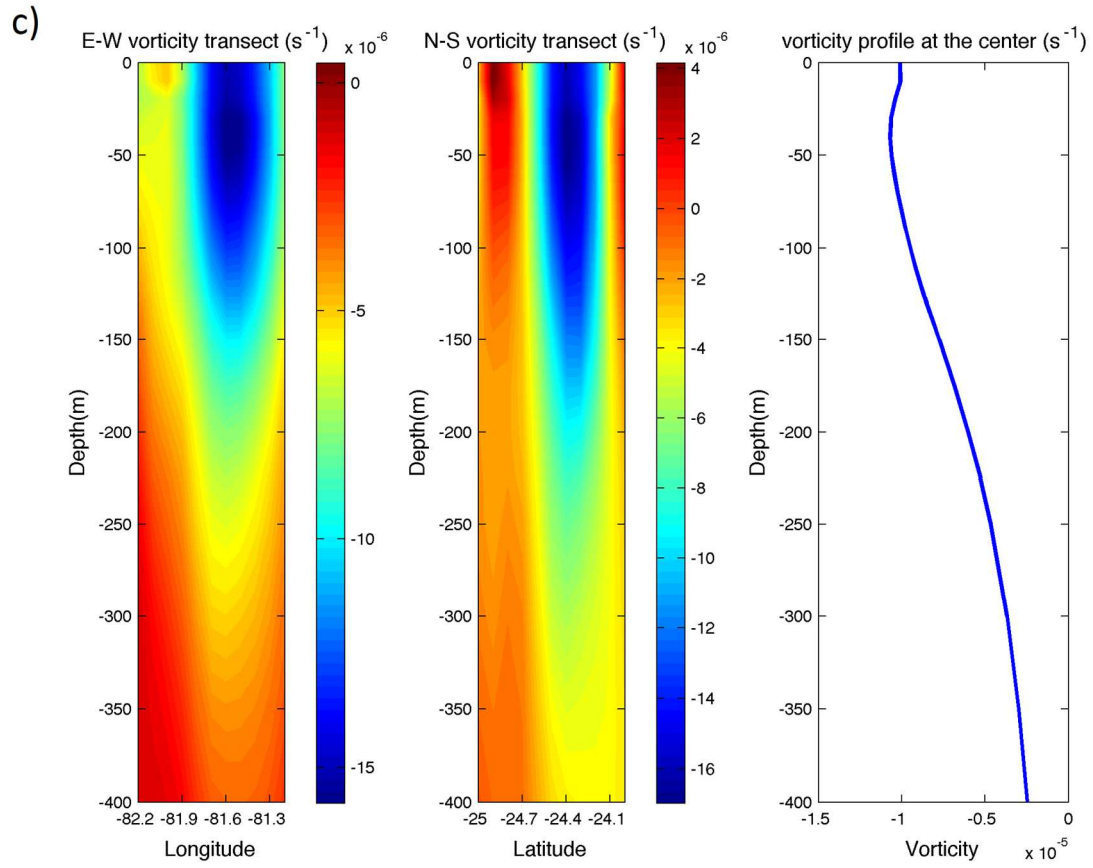


Fig. 7: Map of the index  $\chi_\rho$  (red for positive index and subsurface vortices, blue for negative index and surface vortices) superimposed on the SLA (red lines) in the Peru-Chile area calculated from the fields presented in Fig. 5 (the position of specific eddies analysed in this study is indicated by numbers).







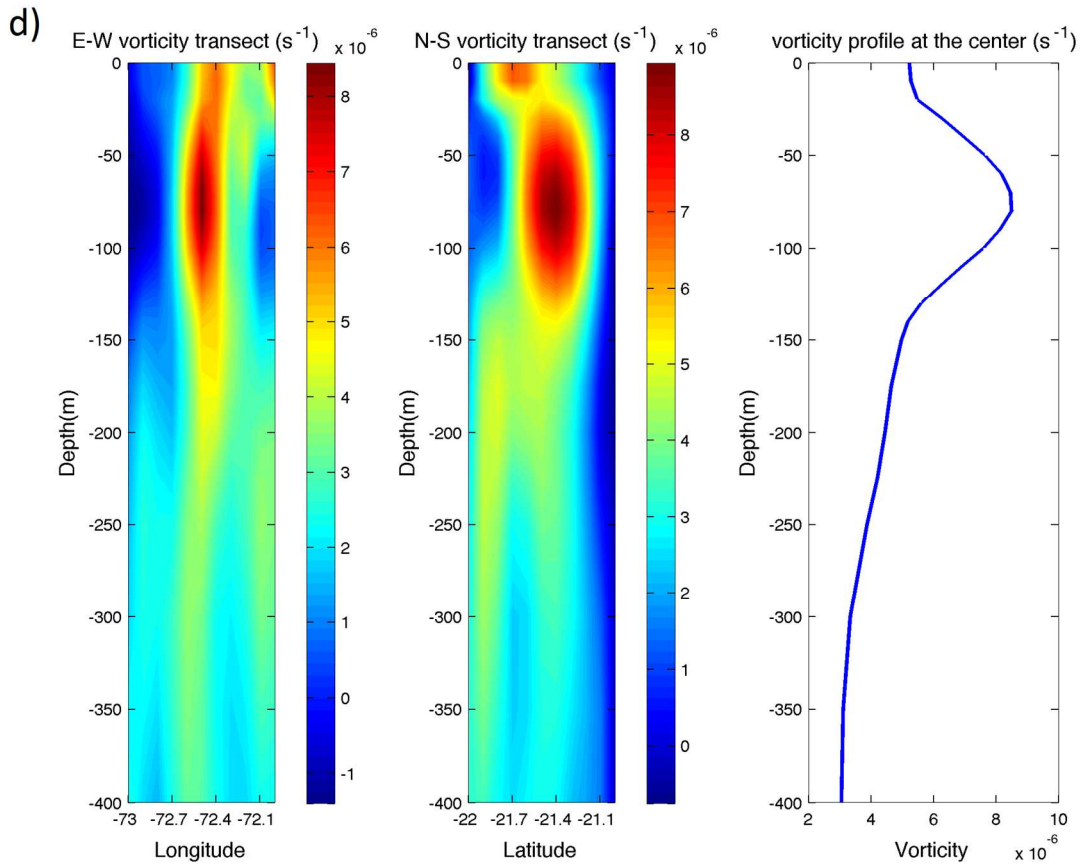


Fig. 8: Relative vorticity (East-West and North-South transects, vertical profile) of eddies correctly identified: a- cyclonic surface eddy, b-anticyclonic surface eddy, c- cyclonic subsurface eddy, d-anticyclonic subsurface eddy. The position of each vortex (denoted 8a, b, c and d) is indicated in Fig. 7.

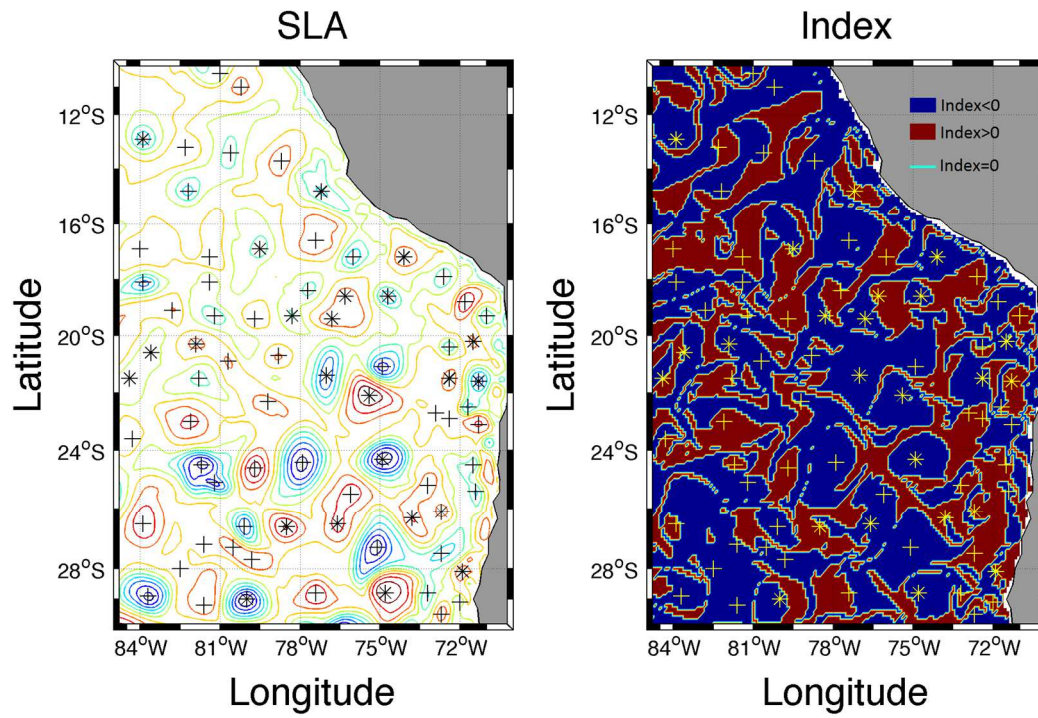
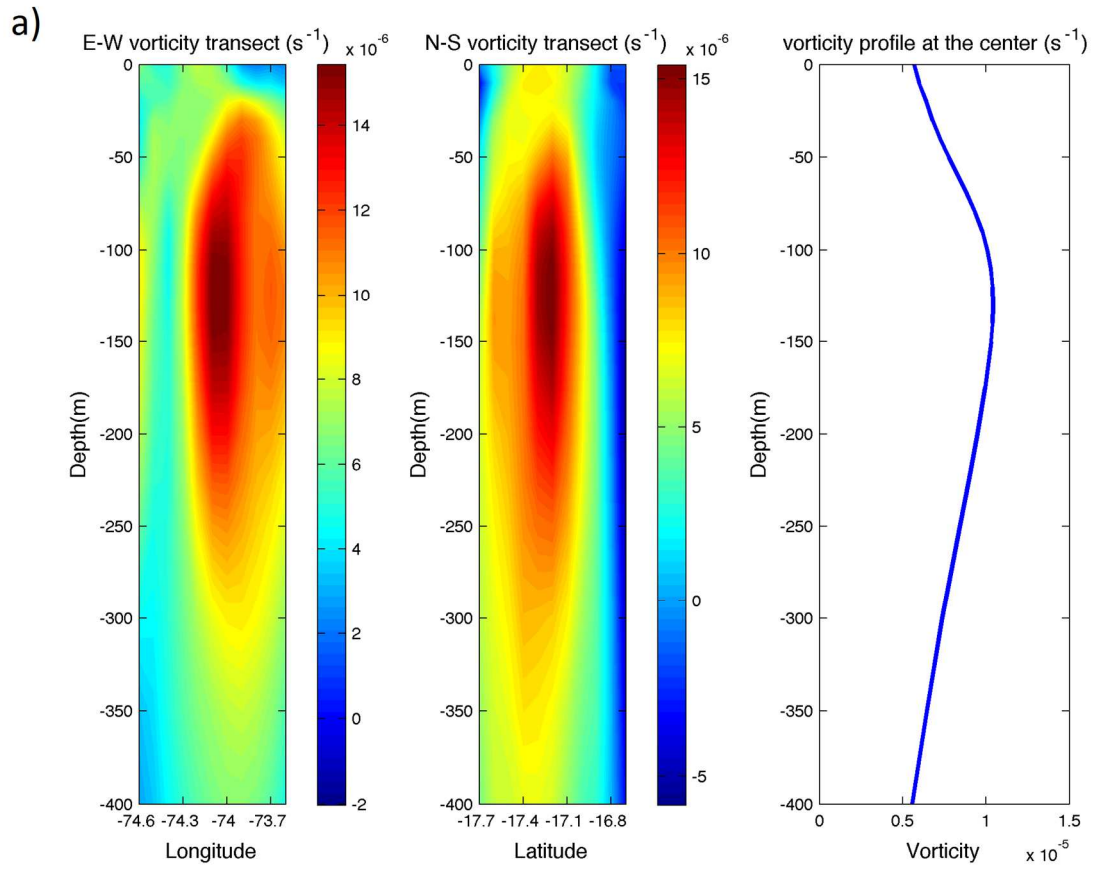
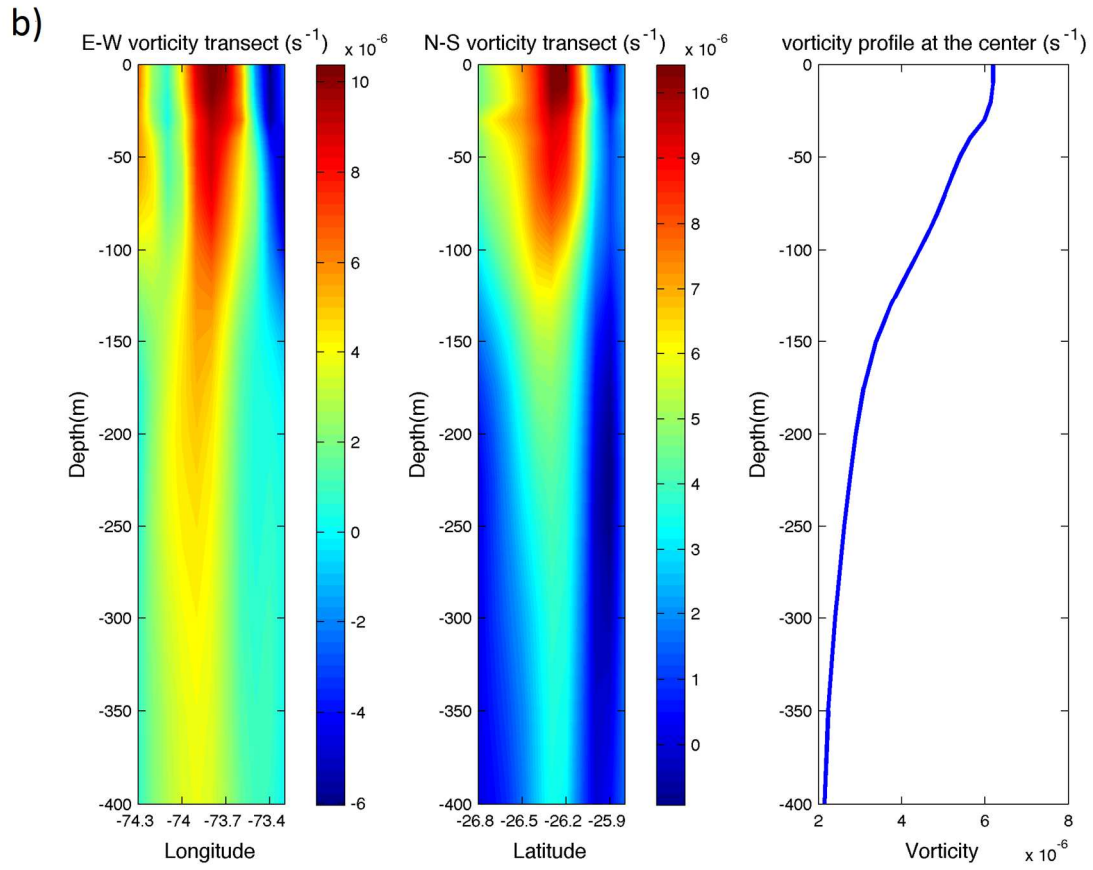
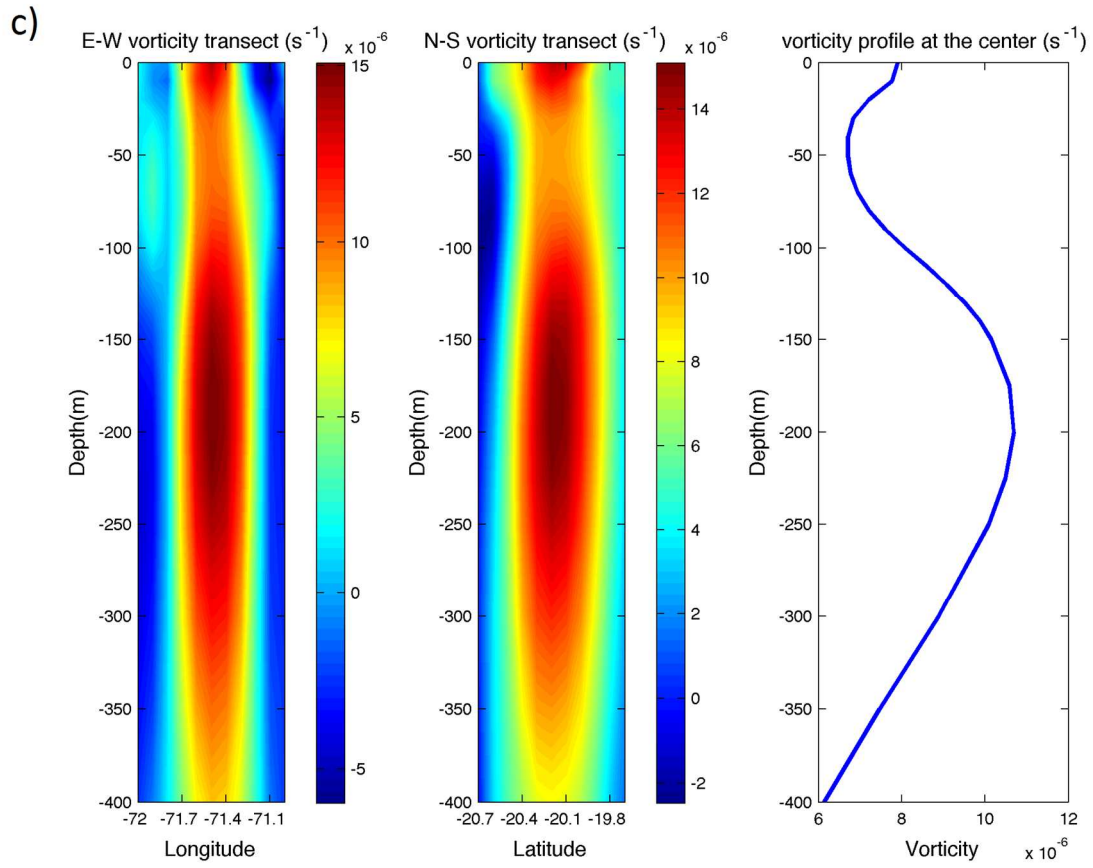


Fig. 9: SLA (left panel, same as Fig. 5a but with fewer contours) and Index  $\chi_p$  (right panel, same as Fig. 7). Eddies that are correctly identified by the index are labelled with crosses (+). Eddies that are not correctly identified by the index are labelled with stars (\*).







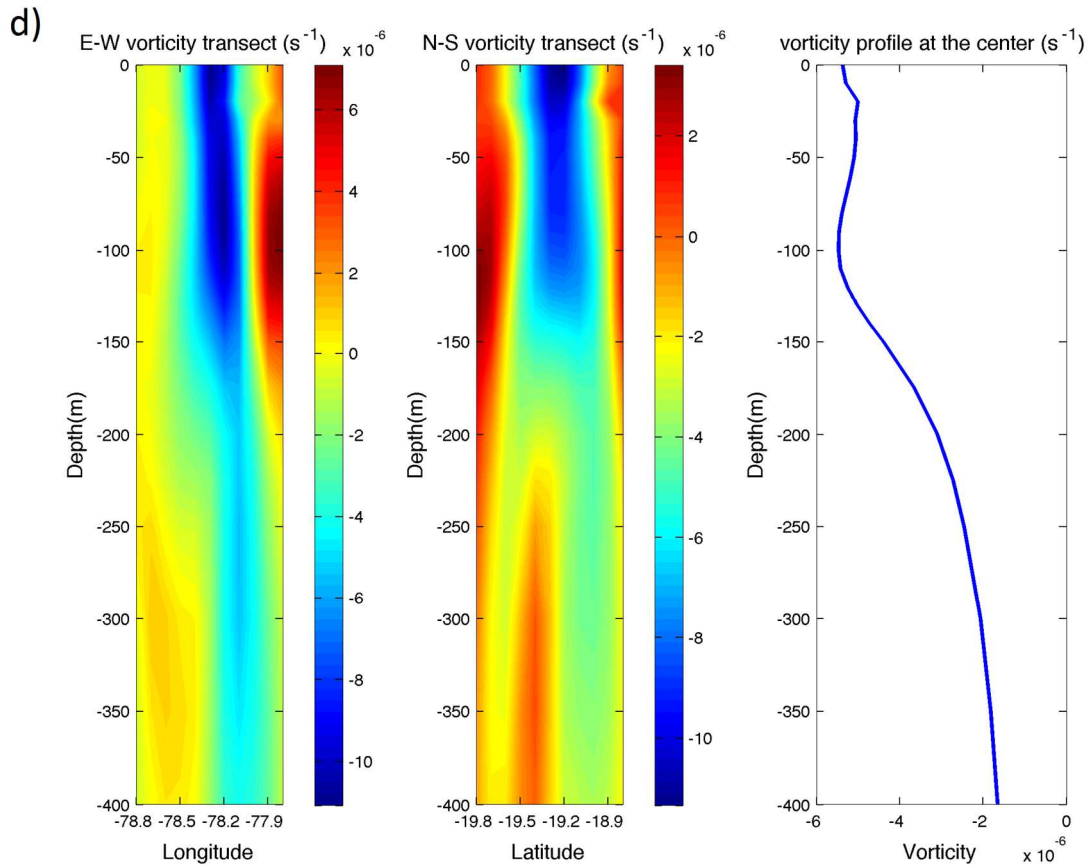


Fig.10: Vorticity structure of the 4 eddies which the index yields wrong results. For each vortex, we have represented the East-West and North-South transects of relative vorticity, and a mean vertical profile near the center. The positions of each vortex (denoted 10a, b, c and d) are also given on Fig.7.

997

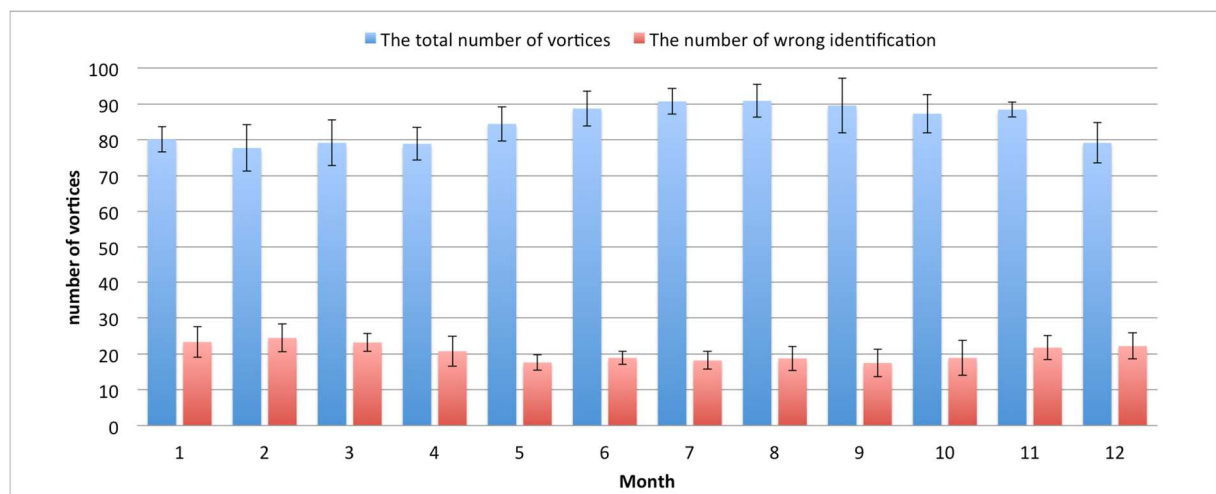


Fig. 11: Diagram representing the monthly statistics of vortices identification for the

numerical simulation used in the study (the black intervals represent the standard deviation for each month over the seven years of simulation).

998

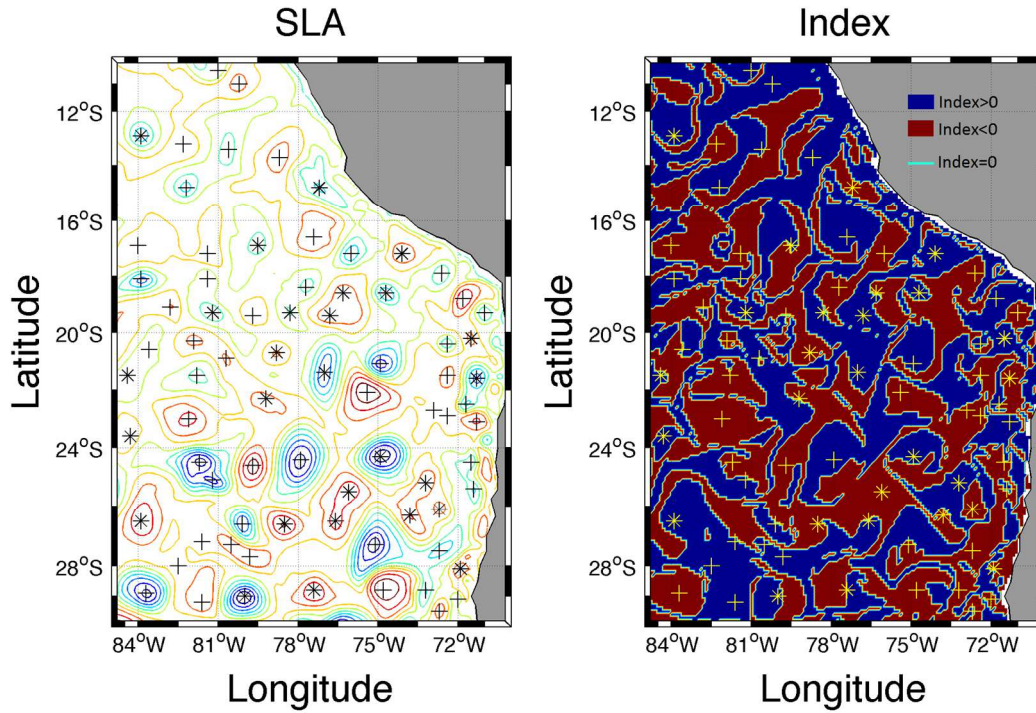


Fig. 12: Same as Fig. 9 but using  $\chi_T$  instead of  $\chi_p$ . Eddies that are correctly identified by the index are labelled with crosses (+). Eddies that are not correctly identified by the index are labelled with stars (\*).

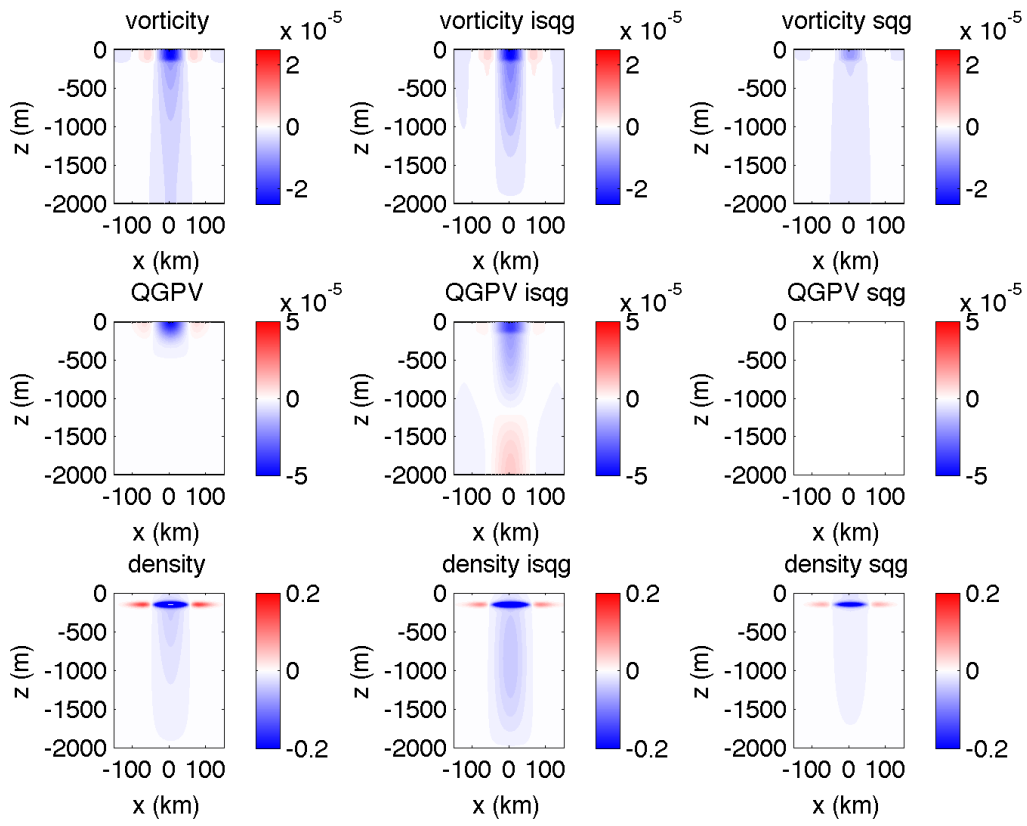


Fig. A.1: Vertical section of vorticity, QGPV and density fields for a surface anticyclone with  $\delta\rho_0 = -0.02 \text{ }^0/_{00}$ ,  $R = 50 \text{ km}$ ,  $H_v = 200\text{m}$ ,  $z_0 = 0\text{m}$  and  $Q_0 = -0.5f$  (left column) and reconstructed fields for ISQG (middle column) and SQG (right column).

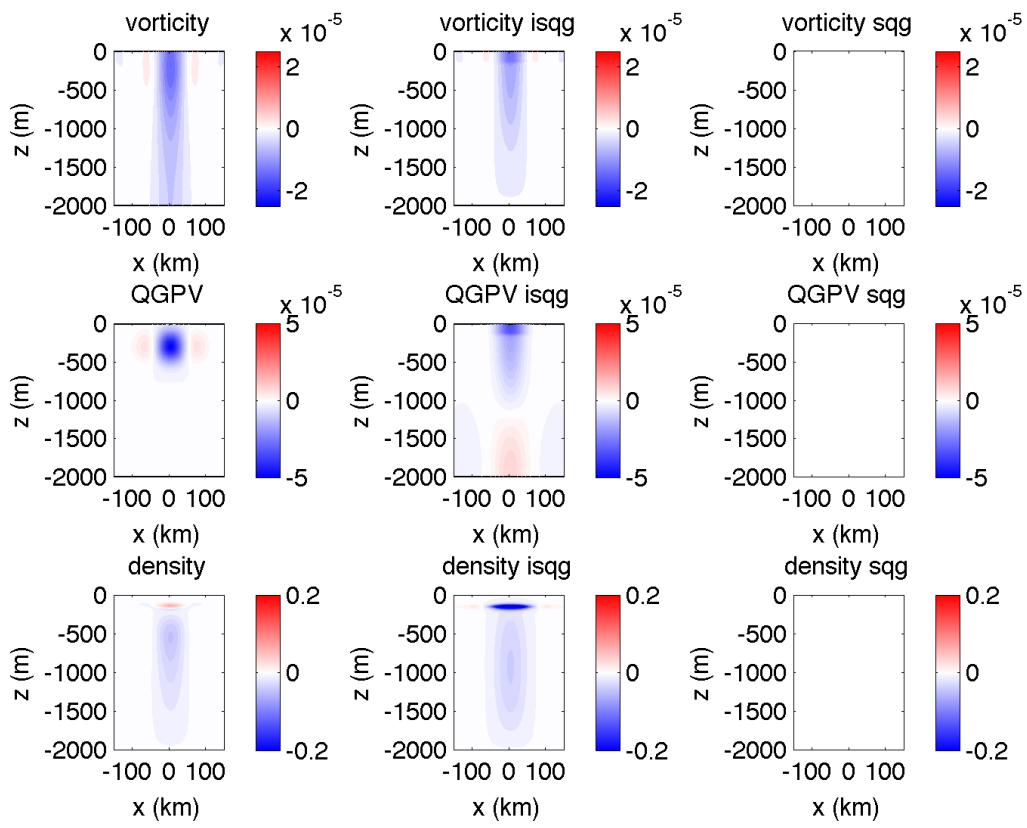


Fig. A.2: Vorticity, QGPV and density fields for a surface anticyclone with  $\delta\rho_0 = 0$ ,  $R = 50$  km,  $H_v = 200$  m,  $z_0 = 300$  m and  $Q_0 = -0.5f$  (left column) and reconstructed fields for ISQG (middle column) and SQG (right column).

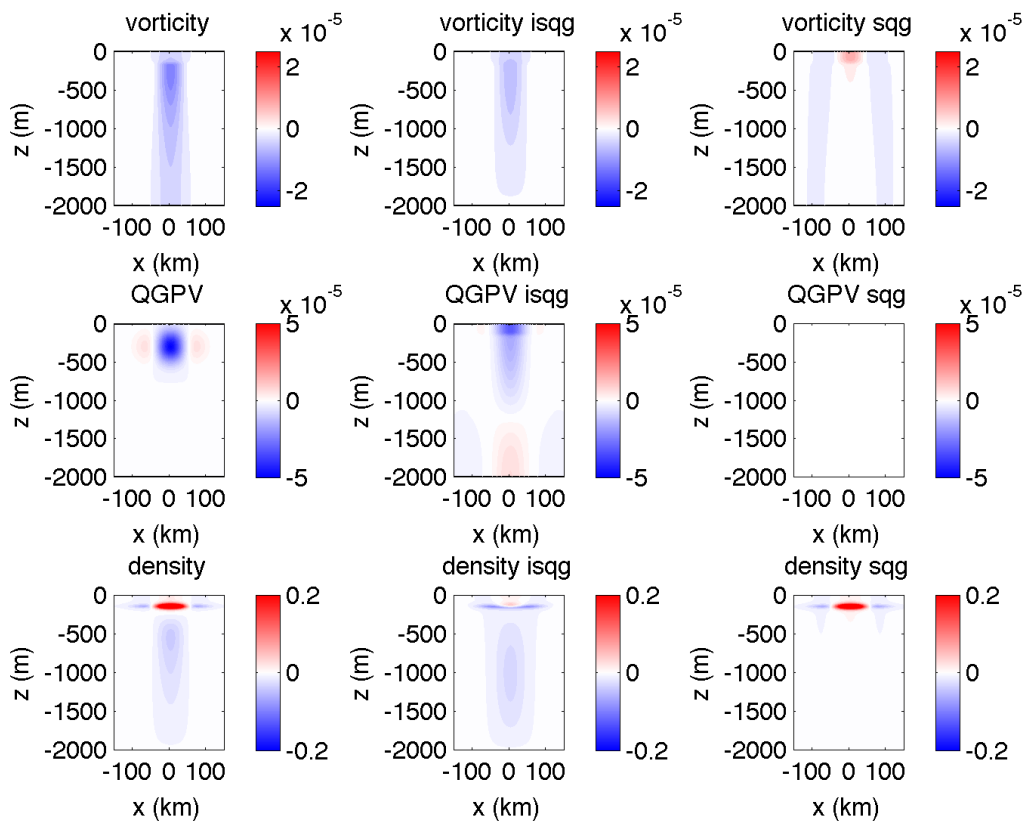


Fig. A.3: Vorticity, QGPV and density fields for a surface anticyclone with  $\delta\rho_0 = 0.02 \text{ } ^0/_{00}$ ,  $R = 50 \text{ km}$ ,  $H_v = 200 \text{ m}$ ,  $z_0 = 300 \text{ m}$  and  $Q_0 = -0.5 f$  (left column) and reconstructed fields for ISQG (middle column) and SQG (right column).